

Deriving flow velocity and initial concentration from Liesegang-like patterns

Chong Liu¹, Victor Calo², Klaus Regenauer- Lieb³, and Manman Hu⁴

¹The University of Hong Kong

²Curtin University

³UNSW Sydney

⁴University of Hong Kong

April 26, 2024

Abstract

Zebra rocks, characterized by their striking reddish-brown stripes, rods, and spots of hematite (Fe-oxide), showcase complex self-organized patterns formed under far-from-equilibrium conditions. Despite their recognition, the underlying mechanisms remain elusive. We introduce a novel advection-dominated phase-field model that effectively replicates the Liesegang-like patterns observed in Zebra rocks. This model leverages the concept of phase separation, a well-established principle governing Liesegang phenomena. Our findings reveal that initial solute concentration and fluid flow velocity are critical determinants in pattern selection and transition. We quantitatively explain the spacing and width of a specific Liesegang-like pattern category. Furthermore, the model demonstrates that vanishingly low initial concentrations promote the formation of oblique patterns, with inclination angles influenced by rock heterogeneity. Additionally, we establish a quantitative relationship between band thickness and geological parameters for orthogonal bands. This enables the characterization of critical geological parameters based solely on static patterns observed in Zebra rocks, providing valuable insights into their formation environments. The diverse patterns in Zebra rocks share similarities with morphologies observed on early Earth and Mars, such as banded iron formations and hematite spherules. Our model, therefore, offers a plausible explanation for the formation mechanisms of these patterns and presents a powerful tool for deciphering the geochemical environments of their origin.

Deriving flow velocity and initial concentration from Liesegang-like patterns

Chong Liu¹, Victor M. Calo², Klaus Regenauer-Lieb^{3,4}, Manman Hu¹

¹Department of Civil Engineering, The University of Hong Kong, Hong Kong, China

²School of Electrical Engineering, Computing, and Mathematical Sciences, Curtin University, P.O. Box
U1987, Perth, WA 6845, Australia

³WA School of Mines: Minerals, Energy and Chemical Engineering, Curtin, Bentley, WA 6102, Australia

⁴School of Minerals and Energy Resources Engineering, UNSW, Sydney, NSW 2052, Australia

Key Points:

- Rich Liesegang-like patterns are replicated by varying flow velocities and initial conditions;
- A new class of inclined bands identified in a very narrow flow velocity and low concentration regime;
- Pattern precisely characterizes flow velocity and concentration when observed;

Corresponding author: Manman Hu, mmhu@hku.hk

Abstract

Zebra rocks, characterized by their striking reddish-brown stripes, rods, and spots of hematite (Fe-oxide), showcase complex self-organized patterns formed under far-from-equilibrium conditions. Despite their recognition, the underlying mechanisms remain elusive. We introduce a novel advection-dominated phase-field model that effectively replicates the Liesegang-like patterns observed in Zebra rocks. This model leverages the concept of phase separation, a well-established principle governing Liesegang phenomena. Our findings reveal that initial solute concentration and fluid flow velocity are critical determinants in pattern selection and transition. We quantitatively explain the spacing and width of a specific Liesegang-like pattern category. Furthermore, the model demonstrates that vanishingly low initial concentrations promote the formation of oblique patterns, with inclination angles influenced by rock heterogeneity. Additionally, we establish a quantitative relationship between band thickness and geological parameters for orthogonal bands. This enables the characterization of critical geological parameters based solely on static patterns observed in Zebra rocks, providing valuable insights into their formation environments. The diverse patterns in Zebra rocks share similarities with morphologies observed on early Earth and Mars, such as banded iron formations and hematite spherules. Our model, therefore, offers a plausible explanation for the formation mechanisms of these patterns and presents a powerful tool for deciphering the geochemical environments of their origin.

Plain Language Summary

Zebra rocks, known for their unique red and brown stripes and spots, hold clues to how similar patterns formed on early Earth and Mars. We have developed a new model to explain how these intriguing patterns form. The model suggests that the flow of fluids and the initial amount and location of dissolved iron-oxide (rust) in water plays a big role in shaping the final Zebra rock design. The speed of the flow and the initial amount of rust can create different stripe and spot patterns, just like the ones in Zebra rocks. By studying these rocks, we can potentially decipher fluid flow scenarios of ancient environments on both Earth and Mars.

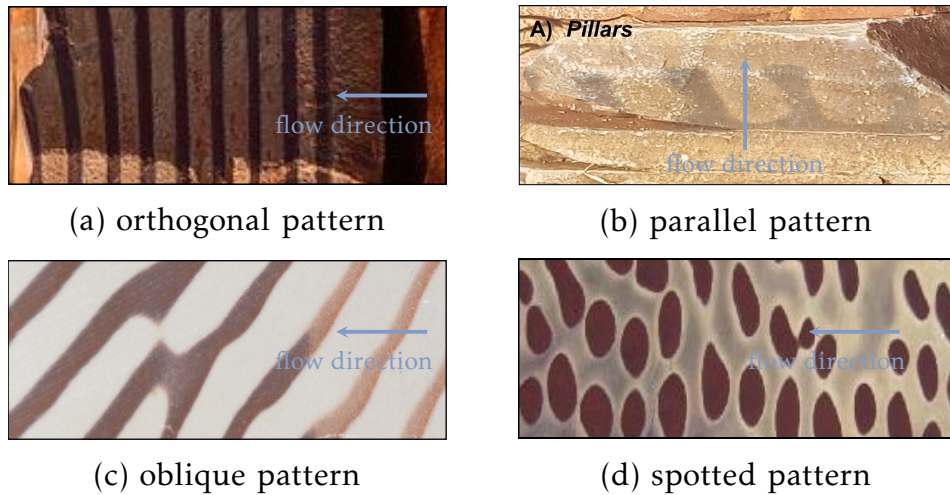
1 Introduction

When geological systems are far from equilibrium, self-organization processes can form geochemical patterns autonomously (Ortoleva et al., 1987; L’Heureux, 2013; Wang et al., 2015; Al-Ghoul & Sultan, 2019; C. Liu et al., 2022, 2023a; Yatsuda et al., 2023; Qiu et al., 2024). Heterogeneity of geological materials and systems as well as complicated boundary conditions can make the observed patterns rich in information about the geological environments in which they are formed, particularly concerning fluid migration and initial conditions. In this contribution we develop a theory and method to use these patterns to provide a window into the past of planetary evolution.

One example of extensively studied pattern formation is the formation of variable hematite (Fe-oxide) on early Earth and Mars, including the Zebra rock formation, Precambrian banded iron formations (BIFs), Mississippi-Valley-type (MVT) ores, and others (Wang et al., 2009, 2015; C. Liu et al., 2023a). Field evidence suggests that groundwater flows influence the formation of Fe-oxide precipitation bands and that BIFs may reflect the changing composition of the oceanic crust (Kawahara et al., 2022; Wang et al., 2009). Additionally, concretions formed in Jurassic Navajo Sandstone have been proposed as a terrestrial analog to hematite spherules detected by the rover Opportunity at the Meridiani Planum site on Mars (Chan et al., 2004; Arvidson et al., 2014; Yoshida et al., 2018). Therefore, a better understanding of the pattern-forming processes in rocks and minerals can reveal valuable information about the geological environment on early

64 Earth and Mars, including the possibility of aqueous environments on Mars and the abil-
 65 ity to invert fluid flow velocity and initial solute concentration on early Earth.

66 We study the Zebra Rock pattern in the northern region of Western Australia, which
 67 exhibits a unique and highly noticeable rhythmic concentration of hematite (Kawahara
 68 et al., 2022). Among all hematite banding patterns, none are as distinct and rich as the
 69 Zebra rock patterns. Thus, the Zebra rock formation is an excellent analog for various
 70 pattern-forming processes associated with subsurface environmental evolution. Zebra rock
 71 formation contains reddish-brown bands, rods, and elliptical spots on a white or light-
 72 colored background, as shown in Figure 1. In our earlier work, we linked Zebra rock for-
 73 mation to the Liesegang phenomenon, a process where supersaturation, nucleation (for-
 74 mation of solid particles), and depletion compete to create banded patterns (C. Liu et
 75 al., 2023a, 2023b). This connection was made because some Zebra rock patterns look sim-
 76 ilar to Liesegang bands. However, classic Liesegang bands typically show increasing band
 77 thickness and spacing as they form. Zebra rocks, on the other hand, exhibit a wider var-
 78 iety of patterns. To differentiate these, we refer to the Zebra rock patterns as Liesegang-
 79 like patterns throughout this study.



80 **Figure 1.** Rich patterns appear in Zebra rocks in the northern region of Western Australia:
 81 (a) orthogonal pattern; (b) parallel pattern (after Coward et al. (2023)); (c) oblique pattern; and
 82 (d) spotted patterns.

83 The fundamental Liesegang precipitation model helps to explain the forming mech-
 84 anism of Zebra rocks (Loughnan & Roberts, 1990; Kawahara et al., 2022; Coward et al.,
 85 2023; C. Liu et al., 2023a). However, there are many other hypotheses regarding their
 86 origin, including alternating sedimentation either in marine environments (Larcombe,
 87 1926) or ripple trough (Geidans, 1981), ferronematic liquid crystals (Mattievich et al.,
 88 2003), acid-sulfate soil weathering in conjunction with redox (Retallack, 2021).

89 Recently, acidic-hydrothermal alterations have been suggested to form Liesegang-
 90 like patterns behind a moving front of concentrated iron (Kawahara et al., 2022). How-
 91 ever, this theory faces several challenges in explaining the diverse Zebra rock patterns:
 92 (i) the Liesegang theory predicts only simple band or ring patterns, while Zebra rocks
 93 exhibit a wider variety, including horizontal, vertical, and slanted stripes; (ii) diffusion-
 94 driven Liesegang patterns typically form over a small area. The theory has difficulties
 95 in explaining the vast, multi-layered patterns observed in the Ediacaran Ranford For-
 96 mation, spanning over 45 kilometers (Coward et al., 2023); (iii) the Liesegang model is

97 limited in explaining pattern shape variations and cannot generate the spotted or rod-
98 shaped patterns commonly seen in Zebra rock formations (Coward et al., 2023).

99 In an earlier contribution, we aimed to overcome some limitations of the Liesegang
100 model, using the Cahn-Hilliard model to describe the mineral precipitation in a phase
101 separation model in binary mixtures (C. Liu et al., 2023a). In this case, stripe patterns
102 with the externally imposed periodicity can be stabilized against coarsening above some
103 critical modulation amplitude. However, two essential questions were raised by this model.
104 First, the diffusion-dominated model may not produce the vast Zebra rocks formation
105 argued by Wang et al. (2015). Fluid transport should be necessary for this giant Zebra
106 rock to form across several kilometers horizontally. Second, while the previous model can
107 produce banded and spotted patterns when varying diffusion coefficient or solute mo-
108 bility, it cannot generate the variable bands photographed in the field, containing hor-
109 izontal, oblique, and vertical stripes. Thus, we investigate whether directional quench-
110 ing can create the observed Liesegang-like patterns. This transport-limited model con-
111 centrates on the phase separation process by neglecting the diffusion of the reactants and
112 focusing on the dominant fluid flow. Consequently, we investigate whether the fluid trans-
113 port velocity and initial conditions uniquely determine the pattern morphology.

114 The phase separation process with advection, where fluid flow transports different
115 components, can generate a wide variety of self-organized patterns in various systems.
116 These include binary alloys, fluid mixtures, polymer blends, and even nanostructured
117 thin films. In material science, controlling this process is crucial for designing nanoma-
118 terials and nanodevices with specific functionalities. For example, researchers can cre-
119 ate regular structures desirable for applications ranging from bioactive implants to poly-
120 mer electronics. In such studies Furukawa (1992) investigated the transition between dif-
121 ferent morphologies (shapes) in a binary mixture by varying the speed of the quench-
122 ing front, the boundary between the separated phases. They observed and classified three
123 main categories: irregular, regular lamellar (layered), and regular columnar morpholo-
124 gies. Since then, researchers have introduced alternative descriptions for these transi-
125 tions, considering factors like dimensionality (2D vs. 3D) (Ishikawa et al., 2022), bound-
126 ary and temperature effects (B. Liu et al., 2000; Ishikawa et al., 2022), and the under-
127 lying mechanisms governing the transitions (Krekhov, 2009; Tsukada & Kurita, 2020).

128 In this contribution we extend the analysis to decipher the geological environments
129 by interpreting geological patterns, particularly pattern formation in Zebra rocks. Al-
130 though the advection-dominated phase separation model is successfully applied in ma-
131 terial science, there are still several research gaps in adopting it in geological pattern for-
132 mation: (i) the mechanism of oblique patterns, one of the most notable patterns, remains
133 unclear; (ii) the morphological transition from one particular pattern to the oblique pat-
134 tern is unexplained; (iii) Liesegang patterns are not replicated by the advection-dominated
135 phase separation even though it commonly occurs in diffusion-dominated formulations;
136 (iv) the association between the migration velocities and the band thickness of the uni-
137 form patterns remains unclear; (v) the plausibility of deriving geological environments
138 by reproducing the pattern appearance in Zebra rocks needs investigation. We seek to
139 fill these research gaps by adopting the working hypothesis of Kawahara et al. (2022) and
140 studying the phase separation of Fe-oxyhydroxide under acidic Fe-bearing fluid trans-
141 port conditions by performing numerical simulations in a two-dimensional setting. Note
142 that the model is not limited to the choice of the specific phase separation reaction. How-
143 ever, if a reaction can be identified, the normalized velocities and concentrations can be
144 quantified further by comparing them to laboratory results of the particular reaction cho-
145 sen. We focus here primarily on the investigation of the effect of the transport velocity
146 and initial Fe-oxyhydroxide concentration on the pattern selection and transitions.

147 The remaining parts of this study are organized as follows. Section 2 presents the
148 Cahn-Hilliard formulation with the convection term, which can capture the phase sep-
149 aration process during mineral precipitation. In Section 3, we first select numerical pa-

150 rameters through a series of convergence studies, and then we conduct parameter stud-
 151 ies regarding the transport velocity and initial Fe-oxyhydroxide concentration to inves-
 152 tigate the pattern selection and transition, especially detailed studies for three different
 153 banded patterns. Eventually, we invert the potential geological pattern by replicating
 154 the field patterns photographed in a few Zebra rock outcrops. Section 4 discusses our
 155 numerical results and suggests potential applications of our model in the future. Finally,
 156 we conclude our study in Section 5.

157 2 Methodology

158 2.1 Cahn-Hilliard model

We adopt a classical Cahn-Hilliard model to study Liesegang-like pattern forma-
 tion in a reaction-advection-diffusion system $A_{(aq)} + B_{(aq)} \rightarrow C_{(s)}$. In our study, two
 reagents A and B denoting Fe-bearing acidic fluid and dolomite, respectively, in our study,
 react and produce C (i.e., Fe-oxyhydroxide). This model captures the phase separation
 dynamics occurring in the wake of the fluid front with the $A+B$ chemical reaction. We
 focus on pattern formation and transition by simulating the dynamics of the phase-separating
 chemical C in our model instead of including its production as we studied in our pre-
 vious model (C. Liu et al., 2023a). Using this model, the reaction product C can be sep-
 arated into low- and high-concentration phases (Antal et al., 1999). The concentration
 contrast between phases leads to the forming of precipitation patterns. In this study, the
 Fe-oxyhydroxide concentration enters an unstable region (a.k.a. spinodal), where it di-
 vides into a low-concentration region (no precipitate) and a high-concentration region
 (precipitate), which is underpinned by the classical Cahn-Hilliard equation (Cahn & Hilliard,
 1958; Cahn, 1961):

$$\frac{\partial c}{\partial t} = -\nabla \cdot \left(\lambda \nabla \frac{\delta F}{\delta c} \right) \quad (1)$$

where c is the concentration of the reaction product C and λ is the diffusive mobility;
 we assign $\lambda = 1$ in current study. Let $\mu = \delta F / \delta c = I'_c + B'_c$ be a generalized thermo-
 dynamic potential that drives the phase separation. The interfacial energy is

$$I_c = \frac{1}{2} \sigma |\nabla c|^2 \quad (2)$$

165 in which σ is a constant relevant to interface sharpness; we set it to $\sigma = 0.5$.

In addition, again for simplicity, we use a Landau-Ginzburg type free energy den-
 sity with two minima corresponding to c_l and c_h and the maximum to $\bar{c} = (c_l + c_h)/2$.

$$B_c = \frac{\varepsilon}{2} (c - \bar{c})^2 - \frac{\gamma}{4} (c - \bar{c})^4 \quad (3)$$

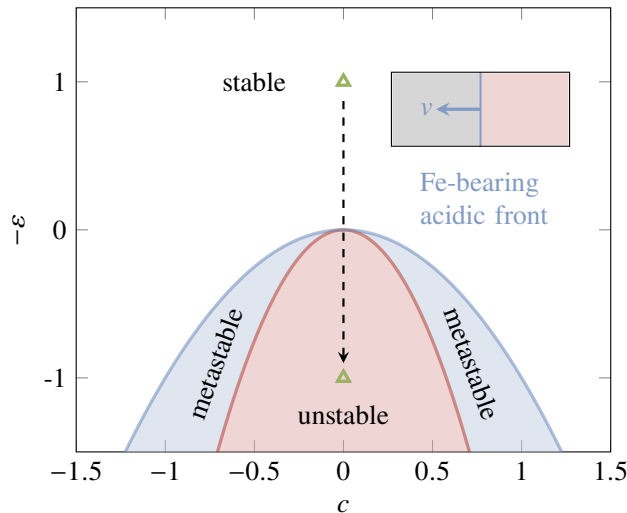
where ε and γ are system-dependent parameters. Here, we assume $\gamma = 1$ and vary the
 parameter ε to control the phase separation process. When $\varepsilon < 0$, the system is sta-
 ble with a single minimum; when $\varepsilon > 0$, the system experiences phase separation with
 two minima. We simply mimic the transport of the Fe-bearing acidic front by varying
 the parameter ε . Initially, we set $\varepsilon = -1$ in the whole system as the static state before
 the Fe-bearing acidic front reaches. During the reactive transport process, the param-
 eter ε varies over both time and space as follows:

$$\varepsilon = \begin{cases} -1, & \text{if } x < vt \\ 1, & \text{if } x \geq vt \end{cases} \quad (4)$$

166 where v is a constant velocity denoting the transport of the Fe-bearing acidic fluid front
 167 and t is time.

Finally, by substituting the chemical potential equations (2) and (3), the Cahn-Hilliard
 equation (1) becomes

$$\frac{\partial c}{\partial t} = \nabla \cdot (\lambda \nabla (-\varepsilon c + \gamma c^3 - \sigma \Delta c)) \quad (5)$$



159 **Figure 2.** Qualitative phase diagram for the phase separation. Phase separation takes place
 160 when $\varepsilon > 0$. The system becomes unstable as $|c| < 1/\sqrt{3}$, while the system is metastable when
 161 $|c| > 1/\sqrt{3}$. The system initially has a negative $\varepsilon = -1$, but the concentration is in the unstable
 162 region. After the Fe-bearing acidic fluid sweeps at constant speed v , we switch $\varepsilon = -1$ to $\varepsilon = 1$.
 163 By doing this, the fluid-swept area will experience phase separation, and different patterns will
 164 emerge. Adapted from Tsukada and Kurita (2020).

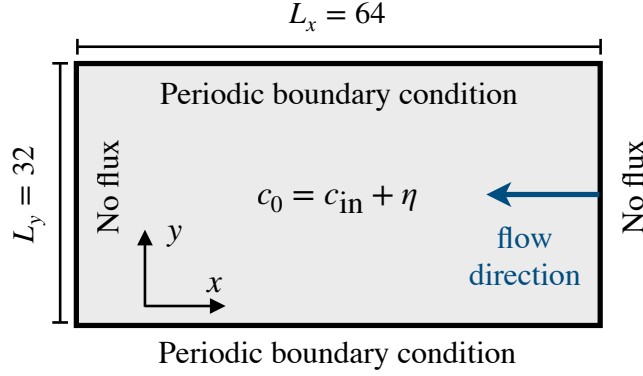
We use a mixed discretization of the system where we avoid the fourth term in the equation (5) by considering the chemical potential μ as an auxiliary variable to facilitate using the standard bilinear finite element space. Then the governing equation (5) separates as

$$\begin{aligned} \frac{\partial c}{\partial t} &= \nabla \cdot (\lambda \nabla \mu) \\ \mu &= -\varepsilon c + \gamma c^3 - \sigma \Delta c \end{aligned} \quad (6)$$

168 2.2 Problem statement

171 We consider an initial-boundary value problem in a rectangular domain Ω as displayed in Figure 3. The domain size is $L_x = 64$ in height and $L_y = 32$ in width, sufficiently large to present different categories of patterns. We impose periodic boundary conditions on the top and bottom edges for both concentration and chemical potential and use the natural boundary condition on the lateral edges. Initially, the product C concentration is set to the stable magnitude, $c_0 = c_{\text{in}} + \eta$ in the whole region, where η denotes noise effects, such as the heterogeneous reagents and thermal fluctuations. We assume η as a random distribution in the range $[-0.01, 0.01]$, a typical value for homogeneous phase-separation simulations (Foard & Wagner, 2012). We put the position of the Fe-bearing acidic fluid front at $x = L_x$. As a result, the whole domain initially remains stable. After the front moves left, the swept region undergoes spinodal decomposition, creating a phase-separating pattern.

183 After determining the boundary and initial conditions, the governing equations (6)
 184 can be solved by PRISMS-PF (DeWitt et al., 2020), which is an open-source, high-performance
 185 phase-field code built on a finite element library `deal.ii` (Arndt et al., 2020). Interested
 186 readers can derive the weak form based on the Cahn-Hilliard implication. In addition,
 187 we use the forward Euler method as the time marching technique. To this end, we should



169 **Figure 3.** Sketch of initial and boundary conditions for Liesegang-like patterns formation
 170 after the infiltration of Fe-bearing fluid flow.

188 select the time increment satisfying the Courant–Friedrichs–Lewy (CFL) condition, which
 189 has been implemented in PRISMS-PF.

190 3 Results

191 We use the Cahn–Hilliard model described in Section 2 to numerically study the
 192 phase separation phenomenon observed in a geological setting. First, we conduct con-
 193 vergence studies in space and time to choose an appropriate mesh size and time incre-
 194 ment in Section 3.1. After selecting the suitable numerical parameters, in Section 3.2,
 195 we perform parameter studies on the speed of the Fe-bearing acidic fluid front as well
 196 as the initial concentration of the product, which plays a decisive role in selecting the
 197 morphology appearance. Finally, Section 3.3 reproduces the different patterns observed
 198 in Zebra rocks by the numerical simulations.

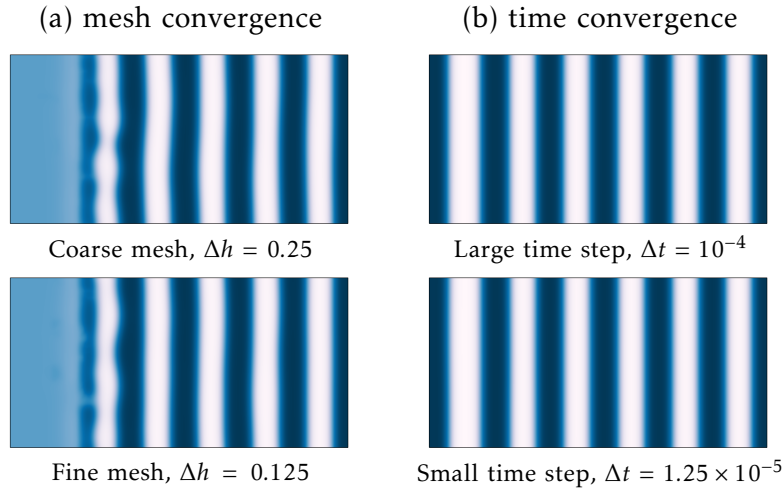
199 3.1 Model convergence study

203 We demonstrate PRISMS-PF’s capability for simulating phase separation problems
 204 by conducting convergence studies in space and time. We perform two simulations for
 205 the mesh size h selection with a fixed time increment $\Delta t = 1.25 \times 10^{-5}$. We vary the
 206 mesh size as $\Delta h = 0.125$ and $\Delta h = 0.25$, respectively. The selections ensure the typi-
 207 cal value, i.e., $\sigma/\Delta h$ ranging from 2 to 4, for the phase field methods capturing the struc-
 208 ture and interfacial evolution. Figure 4a shows that the resulting patterns are similar
 209 except for the localized noise emerging in the transport front. This is because the noise
 210 term is introduced in the initial concentration distribution. Meanwhile, the band loca-
 211 tions match well, demonstrating the noise cannot change the internal characteristics.

212 Additionally, we select the appropriate time step size by performing the temporal
 213 convergence. We fix the mesh size as $\Delta h = 0.25$ but vary the time size as $\Delta t = 10^{-4}$
 214 and $\Delta t = 1.25 \times 10^{-5}$, respectively. The pattern formation after the transport front
 215 approaches the left boundary is depicted in Figure 4b. The reduced time step is in ex-
 216 cellent agreement with the large time step. These results imply that the time size $\Delta t =$
 217 10^{-4} is small enough to guarantee converged results.

218 3.2 Parameter space analysis and patterning

219 We thoroughly explore the parameter spaces to understand better how parameters
 220 affect the pattern formation and transition as the Fe-bearing fluid passes one geologi-
 221 cal formation. We identify the two main parameters responsible for pattern formation



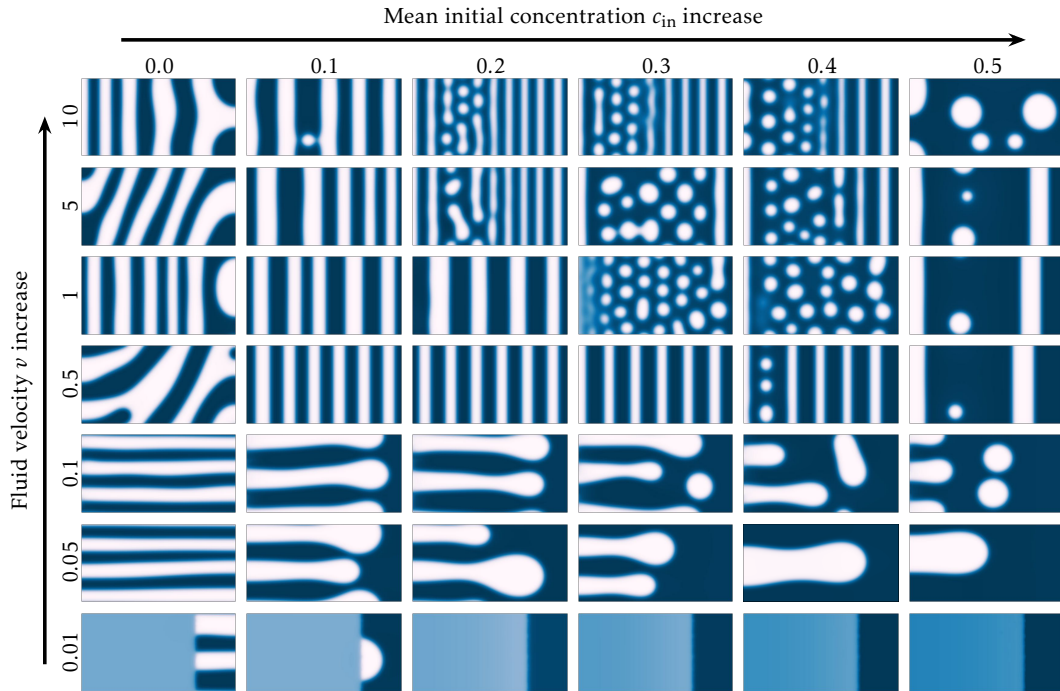
200 **Figure 4.** Convergence studies determining numerical parameters: (a) mesh size and (b) in-
 201 cremental time step. Parameters used in these simulations are $\lambda=1$, $\sigma=0.5$, $\gamma=1$, and ε shifting
 202 from -1 to 1 after the fluid front passes.

222 and selection: the fluid velocity v and initial solute concentration c_{in} . We create a phase
 223 morphology diagram that illustrates the various patterns by fixing one control param-
 224 eter constant while adjusting another. From our simulation results, we initially classify
 225 these patterns into five morphologies by their characteristics and the formed pattern with
 226 the direction of the fluid flow. Subsequently, we assess one category of banded patterns
 227 quantitatively by relating the spacing coefficient with the fluid speed. These simulations
 228 use the same setup as those described in Section 3.1.

229 3.2.1 Morphology phase diagram

235 We numerically examine how the fluid velocity v and initial solute concentration
 236 c_{in} influence the pattern evolution. For the parameter sweep, we consider seven differ-
 237 ent fluid velocities, spanning several orders of magnitude from 0.001 to 10, to ensure the
 238 emergence of all potential morphologies. Additionally, we set the initial solute concen-
 239 tration c_{in} from 0.0 to 0.5 with an increment of 0.1, satisfying the spinodal decomposi-
 240 tion condition with a limit of $c_{\text{in}} < 1/\sqrt{3}$ in Figure 2. As a result, we perform 42 simu-
 241 lations to observe the morphology evolution while varying v and c_{in} , as shown in Fig-
 242 ure 5. It is worth noting that we end each simulation as long as the corresponding pat-
 243 tern shows all the characteristics.

244 First, we classify the patterns that emerge following the phase separation, as the
 245 resulting patterns exhibit great versatility. Drawing upon the features exhibited by these
 246 patterns, we categorize them as banded or spotted patterns, as discussed in our recent
 247 work (C. Liu et al., 2022, 2023a). To avoid any potential confusion, we refer to patterns
 248 with a spotty appearance as spotted patterns. Furthermore, within the banded morpholo-
 249 gies, we further classify them into three distinct categories based on the direction of the
 250 bands relative to the fluid flow: (i) orthogonal bands, characterized by stripes perpen-
 251 dicular to the fluid flow direction; (ii) parallel bands, oriented in parallel with the fluid
 252 front; and (iii) oblique bands, displaying an inclined angle relative to the fluid front. No-
 253 tably, no discernible pattern is observed in some instances referred to as homogeneous
 254 cases. In total, our simulations yield five distinct pattern types. Although this simple
 255 classification of morphologies is based on our numerical findings, it provides a valuable
 256 tool for visually distinguishing patterns observed in geological settings on Earth and Mars (Barge

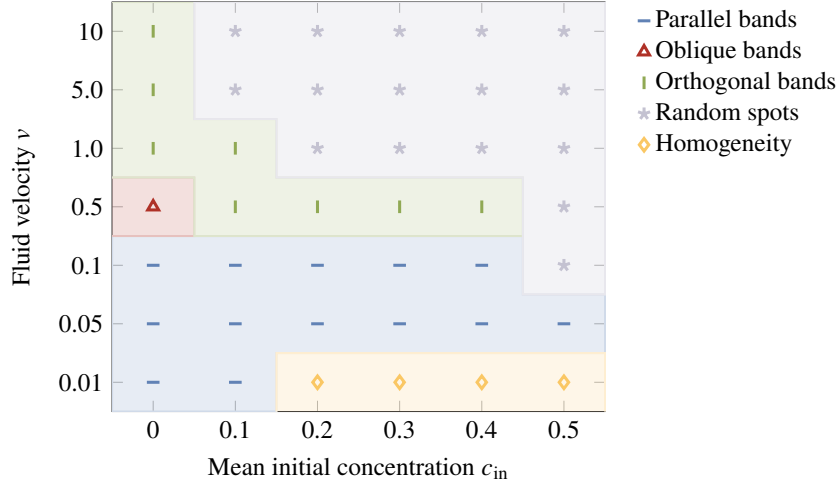


230 **Figure 5.** Morphology evolution in the phase diagram where the initial solute concentration
 231 and fluid front speed are varied.

257 et al., 2011; Wang et al., 2015; Yoshida et al., 2018). An example is the patterns observed
 258 in Zebra rocks (Coward et al., 2023). According to the proposed classification criterion,
 259 we divide the generated patterns into five groups. Figure 6 shows that the fluid velocity
 260 v and initial solute concentration c_{in} are crucial to determining the pattern type.

261 Second, we investigate the effect of the Fe-bearing fluid velocity on the pattern forma-
 262 tion and transition as we can observe the simulated patterns from the bottom to top
 263 in Figure 6, the simulated patterns transition from parallel bands to orthogonal bands
 264 and ultimately to spotted patterns. This transition depends on the initial concentration
 265 level c_{in} . The transition speed from the striped to spotted patterns is particularly sen-
 266 sitive to concentration, with the speed decreasing as c_{in} increases. In contrast, when $c_{in} <$
 267 0.5 , the transition speed from parallel to orthogonal stripes is gentler and remains con-
 268 stant throughout our simulations. Without refined simulations conducted, we report the
 269 trend that the transition velocity tends to decrease between 0.1 and 0.5 as c_{in} increases.
 270 This phenomenon becomes apparent when c_{in} reaches 0.5 , and the front velocity v drops
 271 from 0.1 to 0.05 . Furthermore, homogeneity only arises when the slow velocity is com-
 272 bined with a relatively high initial concentration. Interestingly, oblique bands are only
 273 observed once in our phase diagram, with $c_{in} = 0$ and $v = 0.5$. Given the uniqueness
 274 of this pattern, we provide an in-depth analysis in the following section.

275 Finally, we survey the pattern evolution in the horizontal axis to test the influence
 276 of the initial concentration c_{in} . Unlike the comprehensive spectrum of transitions observed
 277 when varying the Fe-bearing fluid velocity, changing the concentration c_{in} with a fixed
 278 v results in only one discernible transition. However, an exception occurs when $v = 0.5$,
 279 where oblique stripes appear when $c_{in} = 0$. When the transport velocity v is relatively
 280 low, pure parallel patterns emerge, while a transition from orthogonal bands to spots is



232 **Figure 6.** Morphology classification based on the pattern features: homogeneous, banded, and
 233 spotted patterns and the banded patterns relative to the fluid direction: parallel, oblique, and
 234 orthogonal patterns.

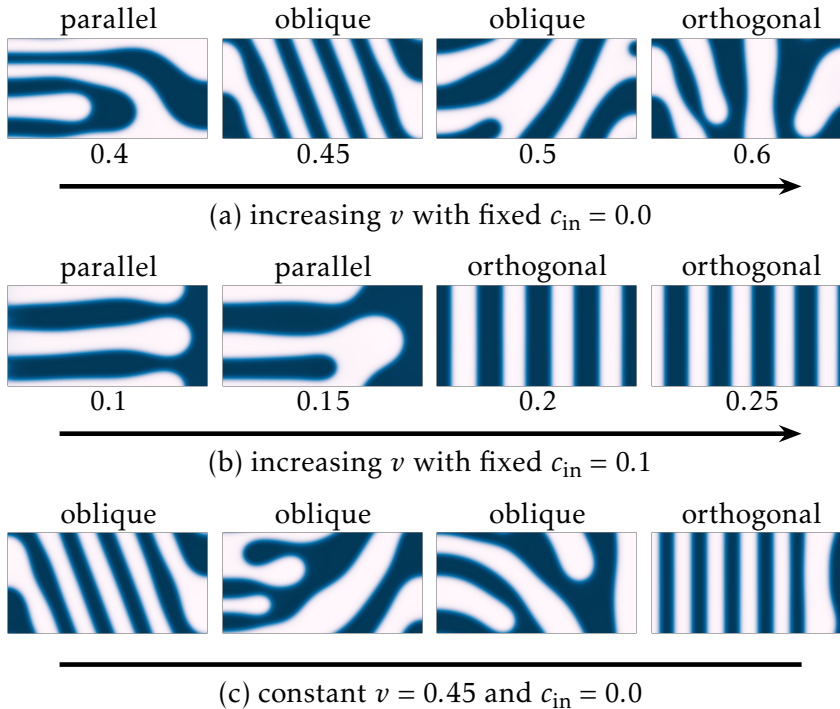
281 observed at higher velocities. Additionally, either parallel or orthogonal bands evolve into
 282 spot morphologies, but a transition between parallel and orthogonal stripes is absent.

283 3.2.2 Oblique band appearance

287 Oblique bands appear in a narrow area with the initial solution concentration $c_{in} =$
 288 0 in the morphology phase diagram. Figure 5 illustrates how the stripe patterns change
 289 from parallel to inclined and ultimately to orthogonal bands when the front speed ac-
 290 celerates from 0.1 to 1.0 with a fixed $c_{in} = 0$. We investigate the transition process by
 291 performing extra simulations with v ranging from 0.4 to 0.6 as Figure 7a shows. There,
 292 oblique patterns emerge at $v = 0.45$ and $v = 0.5$ but with different inclined directions
 293 relative to the fluid front.

294 The arbitrary occurrence of oblique bands is two-fold. First, the creation of the in-
 295 clined patterns depends on the competition between the emergence of parallel and or-
 296 thogonal bands. When the transport velocity reaches a critical value, the competition
 297 becomes comparable. As a consequence, the inclined pattern should appear. Second, this
 298 competitive mechanism explains the varied angles observed in the phase separation pro-
 299 cess occurring in an inhomogeneous system. The heterogeneity is realized by the noise
 300 term that we add in the initial condition. Figure 7c shows that the noise term can dra-
 301 matically affect the morphology selection. In these simulations, the randomly distributed
 302 noise term is the only changing parameter since we maintain the front velocity $v = 0.45$
 303 constant and vanish the initial concentration. Oblique bands with different directions
 304 can appear, even in the form of orthogonal patterns.

305 The initial solution concentration inhibits the occurrence of oblique patterns. As
 306 for the cases of $c_{in} = 0$, we understand that the oblique patterns develop between the
 307 parallel and orthogonal patterns. To test the possibility of inclined patterns when $c_{in} \neq$
 308 0, we capture the transition process from parallel bands to orthogonal bands as nonzero
 309 initial concentrations, e.g., $c_{in} = 0.1$, as Figure 7b shows. Numerical results show that
 310 oblique patterns cannot appear when parallel bands shift to orthogonal bands. The pat-
 311 tern features remain unaltered when we use the same setup as in the convergence stud-



284 **Figure 7.** Pattern formation and selection with increasing front speeds and fixed initial solute
 285 concentration: (a) $c_{in}=0$ and (b) $c_{in}=0.1$. (c) Constant front speed $c_{in}=0.45$ and concentration
 286 $c_{in}=0.0$ with different .

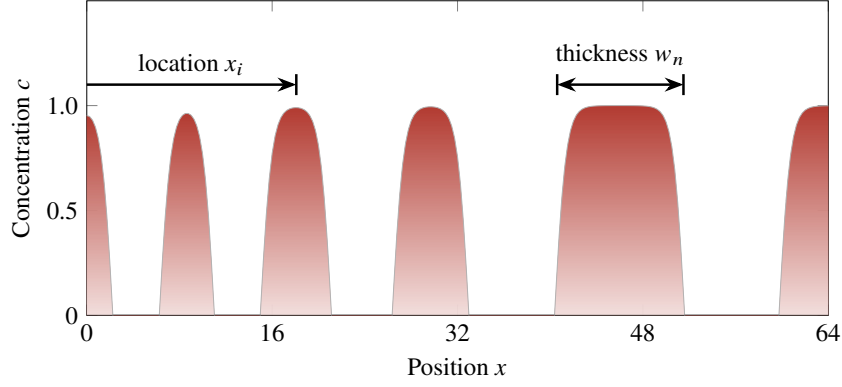
312 ies in Section 3.1. This implies that it is the initial concentration that controls the phase
 313 separation rather than the additional noise term.

314 Overall, the vanishing solute concentration plays a pivotal role in determining the
 315 appearance of oblique patterns, while the noise effect makes the oblique direction emerge
 316 arbitrarily. Our findings explain why randomly oblique patterns can develop in Zebra
 317 rocks in the same geological setting (Coward et al., 2023). Specifically, our study sug-
 318 gests that unprecipitated rocks with heterogeneity tend to develop oblique patterns.

319 3.2.3 *Orthogonal patterns with Liesegang phenomenon*

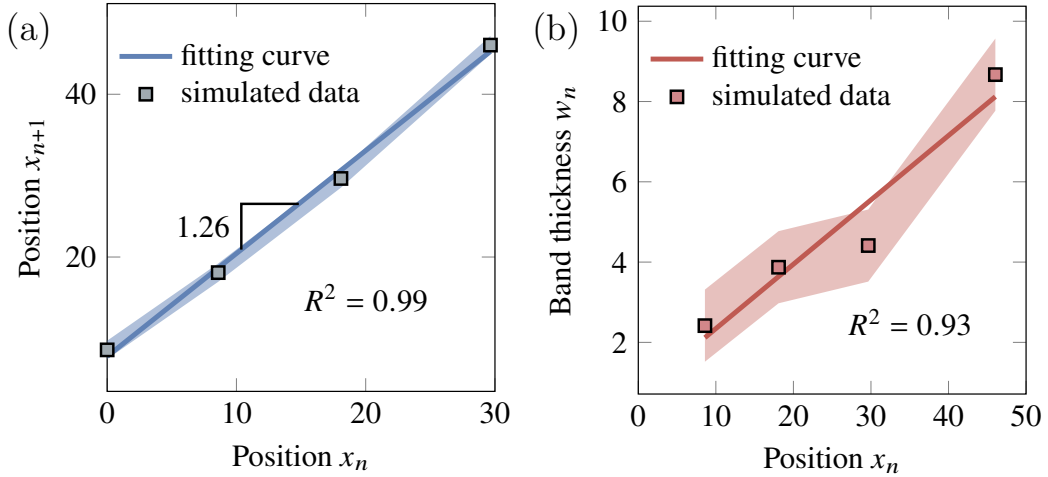
320 In the phase diagram, several orthogonal patterns exhibit characteristics reminis-
 321 cent of the Liesegang phenomenon. As observed in experiments, Liesegang bands are typ-
 322 ically governed by empirical laws regarding their formation time, locations, and widths.
 323 The time law cannot apply in our advection-dominated model since the empirical rela-
 324 tionships are built in the diffusion-limited experiments. However, we seek to quantita-
 325 tively validate the Liesegang-like patterns regarding spacing and width laws by focussing
 326 on a specific combination of $v = 5$ and $c_{in} = 0.1$ in Figure 5. This choice is made based
 327 on the fact that the simulated patterns exhibit behavior closely resembling Liesegang bands.

333 Figure 8 presents the product concentration distribution c along the x -axis follow-
 334 ing the passage of Fe-bearing fluid. As the fluid front propagates, rhythmic precipita-
 335 tion bands appear, forming regular Liesegang band patterns. Qualitatively, the width
 336 of periodic stripes and interband spacing increases, consistent with the behavior of Liesegang
 337 stripes. We quantitatively verify the empirical laws by measuring the band location, e.g.,
 338 i -th band location denoted by x_i , and band thickness, e.g., n -th band thickness repre-



328 **Figure 8.** The product concentration distribution c along the x -axis after the fluid flow, form-
 329 ing the regular Liesegang band patterns. x_i and w_n denote location and thickness of the i -th
 330 and n -th bands, respectively.

339 sented by and w_n . The location x_i represents the distance between the band center and
 the model boundary.



331 **Figure 9.** Verification of Liesegang bands: (a) spacing law and (b) width law. The shaded
 332 regions are the liner regression's root mean square error (RMSE).

340

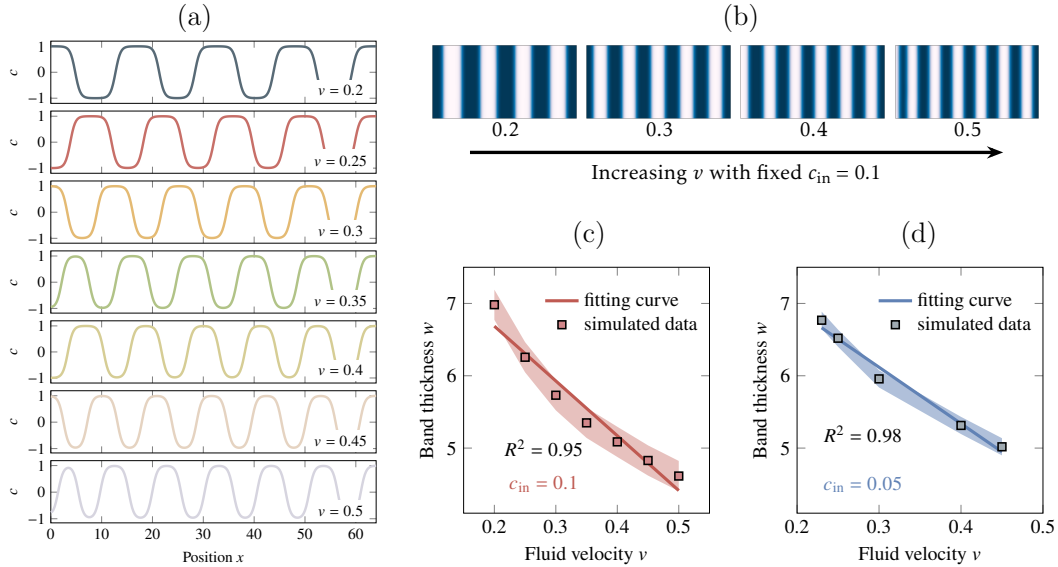
341 We provide quantitative validation for the selected bands and examine the behav-
 342 ior of Liesegang striping in terms of the empirical spacing and width laws. The spacing
 343 law indicates a linear relationship between the locations of subsequent bands, given by
 344 $x_{n+1}/x_n = 1 + p$, where $1 + p$ represents the spacing coefficient. Figure 9a shows this
 345 linear relationship, with a high coefficient of determination $R^2 = 0.99$. The estimated
 346 value of $1+p$ is approximately 1.26, falling within the 1 to 7 range, consistent with the
 347 inversion of Zebra rock samples from the same region (C. Liu et al., 2023a).

348 Additionally, we investigate the width law, which states that the bandwidth w_n is
 349 proportional to the position x_n of the band, i.e., $x_n \propto w_n$. Once again, Figure 9b shows
 350 a linear relation between x_n and w_n . By successfully reproducing these two empirical

351 observations from the Liesegang phenomenon, our simplified model demonstrates the abil-
 352 ity to replicate Liesegang patterns without considering the diffusion of reactants in the
 353 reaction-diffusion system.

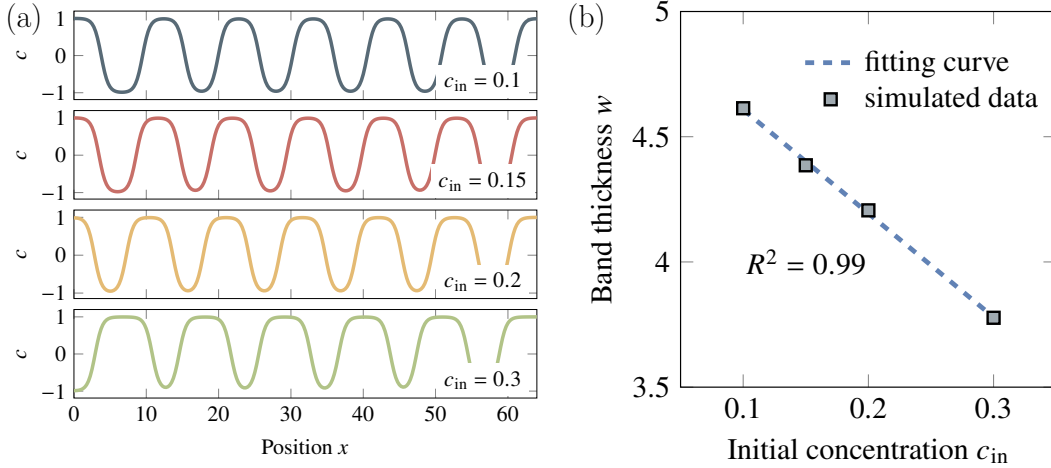
354 3.2.4 Uniform pattern

355 The uniform pattern, commonly observed in Zebra rocks, suggests that the spac-
 356 ing coefficient is around $1 + p \approx 1$, following the classical Turing pattern (Hu et al.,
 357 2022). This study’s uniform pattern refers to orthogonal bands exhibiting minimal strip
 358 variations. Through our simulations, we discover that the diffusion velocity and the initial
 359 concentration influence the bandwidth of each uniform pattern.



355 **Figure 10.** (a) The concentration profiles along the x -axis for varying transport velocities v ,
 356 ranging from 0.2 to 0.5 with a 0.05 increment, while maintaining a constant initial concentra-
 357 tion of $c_{in}=0.1$. (b) The formation of uniform bands at the end of the simulation for four transport
 358 velocities. (c) and (d) The banded thickness measured from the simulations for initial concentra-
 359 tions $c_{in}=0.1$ and $c_{in}=0.05$, respectively, along with the corresponding linear fit.

364
 365 We seek to gain a deeper understanding of the relationship between fluid speed and
 366 band thickness; thus, we conduct refined simulations in the phase diagram, varying the
 367 fluid speed v from 0.2 to 0.5 with 0.05 increments while maintaining a constant
 368 initial concentration of $c_{in} = 0.1$. Figure 10a shows the concentration profiles along the x -axis,
 369 where the bands are located in regions with $c > 0$. Figure 10b illustrates the forma-
 370 tion of regular patterns at four different velocities. The repeated bands exhibit nearly
 371 identical thickness w_n in each simulation. Therefore, we calculate the average band thick-
 372 ness to assess the generated thickness for different front velocities. Subsequently, we plot
 373 the band thickness against the corresponding velocity in Figure 10c. Our results indi-
 374 cate that the band thickness is proportional to the fluid front speed. Specifically, a higher
 375 front speed v leads to a decrease in the band thickness w_n , consistent with the finding
 376 from Yoshida et al. (2020). We conduct five additional simulations for $c_{in} = 0.05$ to val-
 377 idate this linear relationship further. In analogy to the case of $c_{in} = 0.1$, the simula-
 378 tions exhibit the same linear trend as Figure 10d depicts.
 379
 380
 381



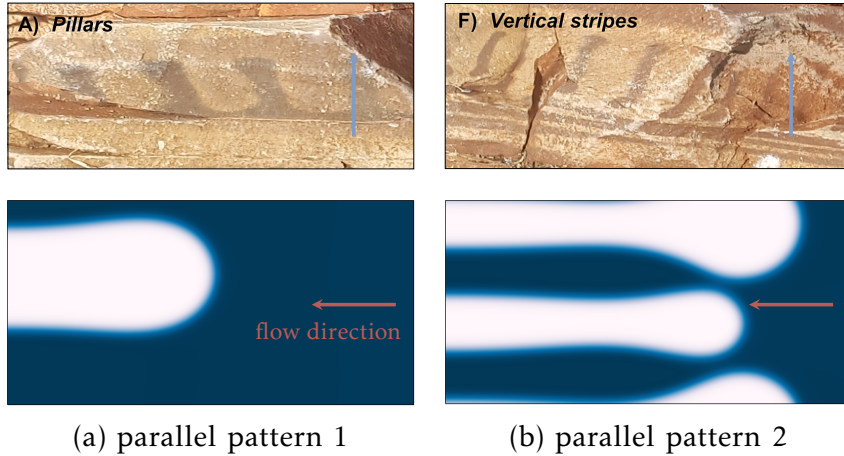
365 **Figure 11.** (a) Concentration profiles along the x -axis for four initial concentrations ranging
 366 from 0.15 and 0.1 to 0.5 with a 0.1 increment with constant transport velocity $v=0.5$. (b) The
 367 estimated banded thickness from the simulations and the corresponding linear fit.

382 The transport velocity and the initial concentration influence the thickness of uni-
 383 form bands. The morphology phase diagram in Figure 5 shows in the column correspond-
 384 ing to $v = 0.5$ for various initial concentrations ($c_{in}=0.1, 0.2,$ and 0.3). We quanti-
 385 tatively investigate this relationship using additional simulations with an initial concen-
 386 tration of $c_{in} = 0.15$ and the same fluid speed of $v = 0.5$. Figure 11a displays the concen-
 387 tration profile along the x -axis, enabling the measurement of the mean band thick-
 388 ness. By determining the average band thickness for each simulation, we can establish
 389 a correlation between the parameter c_{in} and the band thickness, as shown in Figure 11b.
 390 The band thickness decreases as the initial concentration increases, displaying an almost
 391 linear relationship.

392 3.3 Zebra rock pattern comparison

393 This section replicates the hematite patterns observed in Zebra rocks from the West-
 394 ern Australian East Kimberley region. We compare the primary features captured by
 395 our simulations with those present in the field patterns for different pattern classifica-
 396 tions, such as parallel, orthogonal, oblique, and spotted patterns. Our primary focus is
 397 to reproduce the diverse morphologies observed in Zebra rocks. However, a quantitative
 398 analysis is beyond the scope of the current research. For further details, see our recent
 399 work that accurately replicates orthogonal banded patterns in Zebra rocks (C. Liu et al.,
 400 2023a).

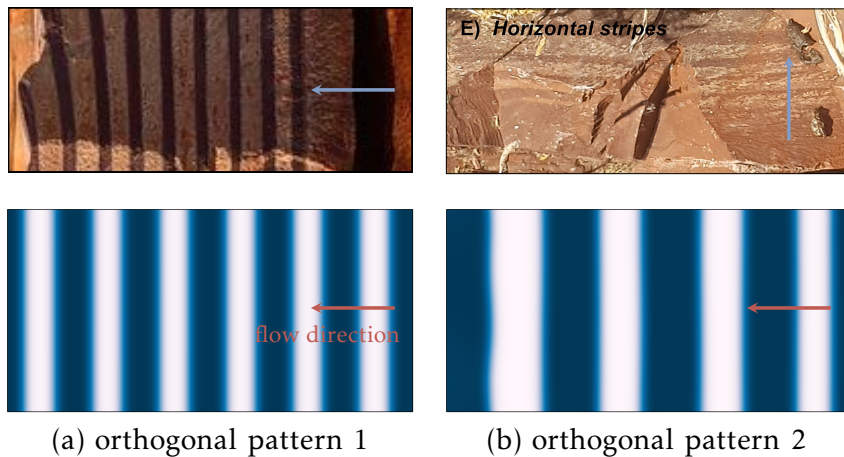
404 *Parallel bands* represent the stripes aligned parallel to the direction of Fe-bearing
 405 flow. Field exploration conducted by Coward and co-authors (Coward et al., 2023) in
 406 four Zebra rock deposits reveals that this pattern is exclusively observed in the Remote
 407 Island outcrop. The researchers identified two representatives within this category: pil-
 408 lars and vertical stripes. Our simulations indicate that these representatives can be clas-
 409 sified as parallel bands with varying propagation lengths. We replicate the two Zebra
 410 rock samples and determine the corresponding flow speeds and initial concentrations by
 411 comparing the simulated morphologies in the morphology phase diagram of Figure 5. The
 412 inverted parameters have the same front velocity $v = 0.05$ and the different initial con-
 413 centrations $c_{in} = 0.5$ for sample 1 and $c_{in} = 0.5$ for sample 2, respectively, as shown
 414 in Figure 12.



401 **Figure 12.** Comparison between the hematite parallel patterns in Zebra rocks and our sim-
 402 ulated patterns. The top two Zebra rock samples are from the Remote Island outcrop, adapted
 403 from Coward et al. (2023). The arrow denotes the Fe-bearing flow direction in each figure.

415 Our inversion indicates that parallel bands emerge under conditions of low fluid ve-
 416 locities. The relatively slow fluid velocity, coupled with a high initial concentration, pro-
 417 motes the formation of elongated strips. On the other hand, a low concentration facil-
 418 itates the development of flat stripes. Consequently, our findings suggest that the trans-
 419 port velocity in the Remote Island outcrop may be relatively sluggish compared to other
 420 locations. Furthermore, inhomogeneous initial conditions can give rise to the simulta-
 421 neous occurrence of both elongated and flat bands.

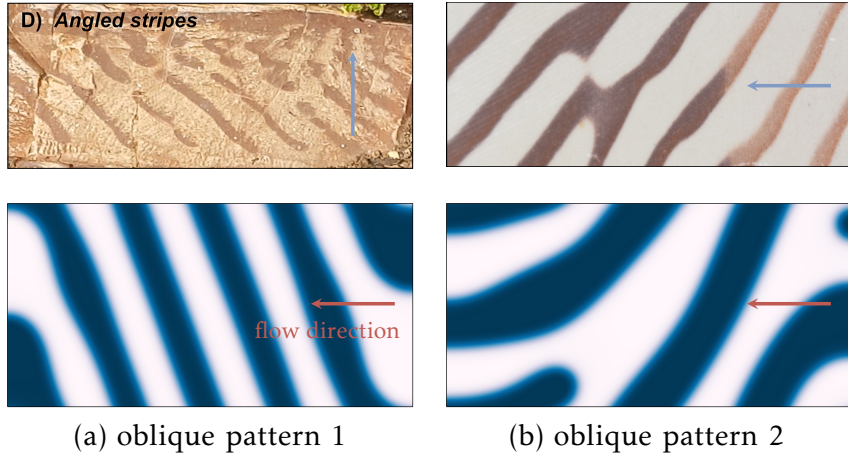
425 *Orthogonal bands* are perpendicular to the fluid direction, commonly observed in
 426 various outcrops. Based on field observations, two orthogonal stripes can be distinguished
 427 in Figure 13. The first group consists of uniform bands with nearly uniform band thick-
 428 ness, as discussed in Section 3.2.4. The second group comprises Liesegang strips that ex-
 hibit an increasing bandwidth along the flow direction, as Section 8 describes.



422 **Figure 13.** Comparison between the hematite orthogonal patterns in Zebra rocks and our
 423 simulated patterns. The top-right Zebra rock sample is located at the Donkey Road deposit,
 424 while the top-right one is from the Remote Island outcrop, adapted from Coward et al. (2023).

429 Following the same procedure as in the previous comparison, we identify the cor-
 430 responding orthogonal stripes that resemble the field morphologies in Figure 5. For the
 431 uniform bands, parameters $v = 0.5$ and $c = 0.2$ produce a similar pattern as shown
 432 in Figure 13. When the velocity is increased to $v = 1.0$ while keeping $c = 0.2$ constant,
 433 our simulation results in a Liesegang pattern. Thus, although we compare field and simu-
 434 lated patterns visually, a quantitative analysis is possible, e.g., in C. Liu et al. (2023a).
 435 Nevertheless, by exploring the morphology phase diagram in Figure 5, we deduce that
 436 the uniform bands indicate a lower transport velocity than the Liesegang patterns. Thus,
 437 our study might suggest that the transport velocity for the uniform pattern observed in
 438 Donkey Road is lower than that for the Liesegang bands observed in the Remote Island.

442 *Oblique bands* are stripes inclined relative to the fluid front, as Figure 14 depicts.
 443 The appearance of oblique patterns occurs in field observation and analogous simulations.
 444 Previously, we explained this pattern as a consequence of curved diffusion directions (C. Liu
 445 et al., 2023a), which could be applicable in specific geological situations. However, this
 446 study relaxes the constraint of curved transport velocity for the inclined stripes, allow-
 447 ing them to emerge more efficiently, mimicking a geological setting. Alternatively, the
 448 competition between parallel and orthogonal bands could contribute to the forming of
 oblique bands, as suggested by the transition morphology in Figure 5.



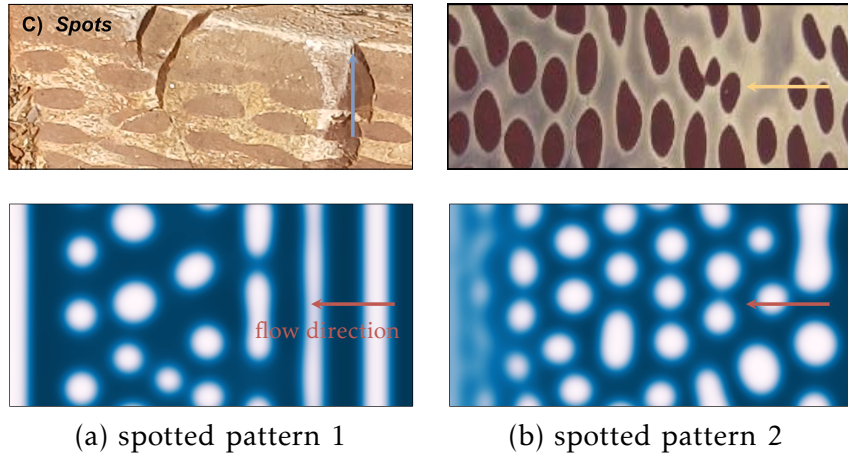
(a) oblique pattern 1

(b) oblique pattern 2

439 **Figure 14.** Comparison between the hematite oblique patterns in Zebra rocks and our simu-
 440 lated patterns. The top-right Zebra rock sample is from the Remote Island outcrop (after Coward
 441 et al. (2023)), while the top-right one is photographed from the Western Australia Museum.

449
 450 Next, we investigate parameter combinations for two Zebra rock samples from the
 451 Remote Island and the Western Australian Museum. Figure 14 demonstrates that fluid
 452 transport velocities of $v = 0.45$ and $v = 0.5$, along with a vanishing initial concentra-
 453 tion $c_{in} = 0.0$, yield comparable oblique bands in the two Zebra rock samples. Inter-
 454 estingly, the field pattern exhibits a branching behavior in some bands, which is also cap-
 455 tured in our results in Figure 14b. Furthermore, while two velocities explain different
 456 patterns in our study, the presence of oblique patterns is heavily influenced by the noise
 457 term η , as Figure 7c shows. Consequently, velocities ranging from 0.45 to 0.5 will likely
 458 result in oblique patterns, with the inclined angle pattern depending on the initial noise
 459 distribution. Nevertheless, the narrowed range of velocities may provide insight into the
 460 potential geological environments during the formation of oblique patterns.

464 *Spotted patterns* combine stripes and spots and patterns consisting solely of spots.
 465 Figures 15a and 15b depict the two types of spotted patterns: (i) stripes that separate
 466 into connected spots and (ii) fully developed isolated spots. Our simulations indicate that
 467 higher fluid speeds contribute to the emergence of mixed patterns. Furthermore, the spot-
 468 ted patterns tend to appear when the initial concentration c_{in} falls within the range of
 0.2 to 0.4, and the fluid speed v exceeds 0.5.



461 **Figure 15.** Comparison between the hematite spotted patterns in Zebra rocks and our simu-
 462 lated spots. The top-right Zebra rock sample is from the Remote Island outcrop (after Coward et
 463 al. (2023)), while the top-right one is located at the Donkey Load deposit.

469
 470 Our simulated morphologies determine the optimal parameters to produce mor-
 471 phologies similar to those in the Museum samples are $v = 5.0$ and $c_{\text{in}} = 0.4$ for sam-
 472 ple 1 of the Remote Island, and $v = 1.0$ and $c_{\text{in}} = 0.4$ for sample 2 of the Donkey Road.
 473 The quantified parameters suggest that the transport velocity in Donkey Road is lower
 474 than that for the Liesegang bands observed in the Remote Island. Additionally, our model
 475 successfully simulates the Ostwald ripening phenomenon, where the stripes separate into
 476 connected and isolated spots in both simulations. This phenomenon plays a crucial role
 477 in the pattern transition observed in Zebra rocks, as discussed in our recent work (C. Liu
 478 et al., 2023a).

479 4 Discussion

480 In this contribution we explored a new framework to explain the diverse patterns
 481 observed in Zebra rocks. This framework builds on the idea of self-organization through
 482 a process similar to the Liesegang phenomenon, where chemicals organize themselves into
 483 bands. Our approach combines the Liesegang theory with a concept from material sci-
 484 ence called phase separation. We modify a well-established model (Cahn-Hilliard) by adding
 485 the effect of flowing groundwater (advection) to mimic how iron oxide dissolves and moves
 486 through rock. This improved model successfully reproduces the variety of patterns seen
 487 in Zebra rocks. The model reveals that it is important to distinguish these Zebra rock
 488 patterns from classic Liesegang bands. Classic Liesegang patterns typically have bands
 489 or rings that increase in width and spacing as they move away from their starting point.
 490 Zebra rocks, however, exhibit a much wider range of patterns, including bands, rods, and
 491 ellipses. We therefore refer to them as Liesegang-like patterns.

492 For the transport-limited case the observed morphological variations between the
 493 Liesegang-like patterns identify differing geological environments during the pattern-forming
 494 process, emphasizing just two factors: the initial solute concentration c_{in} and the fluid
 495 flow velocity v . By systematically examining the parameter space of c_{in} and v using our
 496 model, we can generate all variations of the Liesegang-like patterns previously identified.
 497 However, the impact of geological parameters on the band characteristics varies depend-
 498 ing on the specific category of Liesegang-like patterns being considered. For example,
 499 an oblique banding occurrence most probably indicates the vanishing initial solute con-
 500 centration before the infiltration of acidic iron-bearing fluids. When the Fe-bearing fluid
 501 flow speed narrows to a limited region, the oblique patterns emerge due to the compet-
 502 ing growth of orthogonal and parallel bands. Additionally, the arbitrary inclination an-
 503 gles of the oblique bands may be attributed to the heterogeneous geological conditions
 504 represented by the noise term when setting the initial solute concentration vanish. Our
 505 findings provide insight into the development of randomly oblique patterns observed in
 506 Zebra rocks at five outcrop locations (Coward et al., 2023).

507 One of the categories of orthogonal bands obeys the spacing and width laws com-
 508 monly observed in traditional Liesegang banding. We have previously replicated this type
 509 of pattern, referred to as Liesegang banding, using a pure diffusion-based Cahn-Hilliard
 510 formulation. However, we still classify it as a type of Liesegang-like pattern because the
 511 advection-based formulation annihilates the time law which is primarily governed by diffusion-
 512 limited transport (C. Liu et al., 2022). Our simulations reveal that multiple bands emerge
 513 behind the advection front, unlike the classic Liesegang phenomenon, where band thick-
 514 ness increases step by step. The Ostwald ripening process gradually causes neighboring
 515 bands to coarsen, eventually leading to characteristics similar to those observed in Liesegang
 516 banding.

517 The existence of a linear correlation between the uniform thickness of orthogonal
 518 bands and two controlling parameters presents a valuable opportunity for interpreting
 519 the geological context. Our simulations indicate that the band thickness decreases lin-
 520 early with increasing fluid speed; a similar correlation can be found with the initial so-
 521 lute concentration, too. These quantitative relationships allow us to estimate the fluid
 522 flow rates and initial concentrations based on photographic images captured in the field.
 523 However, a quantitative comparison of the field patterns with the simulated morphologies
 524 is out of the scope of current study. The operational procedure for deriving the dif-
 525 fusion coefficient from orthogonal Zebra rock patterns has been extensively demonstrated
 526 in our earlier work (C. Liu et al., 2023a).

527 The rods and ellipses observed in Zebra rock likely represent an intermediate Ost-
 528 wald Ripening stage, wherein stripes gradually localize into spots or individual spots coarsen
 529 into more prominent spots over time. The former is likely a result of the imposed het-
 530 erogeneity. At the same time, the latter serves to reduce overall system energy, where
 531 combined rods or ellipses are energetically favorable compared to smaller individual spots (Ostwald,
 532 1902). Although our phase separation model can replicate irregular pattern categories,
 533 we cannot exclude the possibility of geological deformation occurring after pattern for-
 534 mation (Sheldon & Retallack, 2001; Retallack, 2021). For instance, formation compaction
 535 may cause spheroids to reduce, resulting in an elliptical shape, a common occurrence in
 536 geological settings. Additional field and experimental work is necessary to confirm the
 537 potential impact of compaction on pattern formation.

538 The examined Zebra rock outcrops exhibit distinct pattern features that have the
 539 potential to provide valuable information about chemical conditions and iron transport.
 540 First, parallel and orthogonal patterns can be observed in different layers of the Ran-
 541 ford formation, attributed to variations in the infiltrating flow rate into the rock. Re-
 542 ferring to the morphology phase diagram (see Figure 5), we can interpret that the fluid
 543 flow rate in the parallel banding layer is lower than that in the orthogonal layer. Ma-
 544 terial heterogeneity, such as permeability, may contribute to these differences in flow rate,

545 as the patterns are bounded by bedding planes. Similarly, inhomogeneous initial con-
 546 ditions can give rise to the simultaneous occurrence of both elongated and flat bands ob-
 547 served in the Remote Island. Furthermore, the variations in pattern features can be used
 548 to infer the flow conditions during the pattern formation process.

549 Zebra rocks, while beautiful and often used as decorative stones, hold a deeper se-
 550 cret. Understanding the patterns of hematite (iron-oxide) within them can unlock valu-
 551 able geological information. These patterns reveal the complex interplay between chem-
 552 ical reactions and fluid movement that shaped the rock. Similar processes may have been
 553 at work in the distant past, creating features like the early Earth's banded iron forma-
 554 tions (BIFs) and the hematite spherules found on Mars. For instance, iron oxide spots
 555 and rods found in Earth's Navajo Sandstone are considered a close match to hematite
 556 nodules on Mars (Chan et al., 2004; Yoshida et al., 2018). The insights gained from study-
 557 ing Zebra rocks may therefore provide valuable tools for interpreting data and poten-
 558 tially even detecting signs of past life on Mars.

559 The Precambrian Banded Iron Formations (BIFs) show three scales of bandings
 560 that may have self-organizational origins (Wang et al., 2009). Understanding how Ze-
 561 bra rock patterns form has significant implications beyond just Zebra rocks themselves.
 562 It can help us unlock secrets about Earth's history and potentially guide resource ex-
 563 ploration. BIFs, similar to Zebra rocks in pattern formation but with a higher iron con-
 564 tent, are commercially valuable for iron ore. By studying Zebra rocks with our model,
 565 methods that identify promising BIF deposits using aerial photographs or drone images
 566 may be developed. This could be a game-changer for resource exploration. The abun-
 567 dance of BIFs in the Archaean and early Proterozoic eras, followed by their decline, sug-
 568 gests a significant shift in the ocean environment. Using our simulations to translate ob-
 569 served patterns into geological parameters guides the potential development of entirely
 570 new geophysical tools. These tools could help us reconstruct the conditions on early Earth's
 571 crust, offering a glimpse into our planet's distant past.

572 5 Conclusion

573 This study delves into the intriguing patterns found in Zebra rocks, focusing on how
 574 these patterns form over time. We use a computer model that simulates the separation
 575 of iron oxide (hematite) under flowing water (advective phase separation). This model
 576 provides valuable insights into how two key factors influence the shapes and transitions
 577 of these patterns: (i) how the iron oxide is initially distributed within the rock affects
 578 the resulting patterns; (ii) the speed at which water moves through the rock plays a role
 579 in shaping the patterns.

580 Using our simulations, we were able to categorize the resulting patterns (referred
 581 to as Liesegang-like patterns) and quantify the influence of the two factors mentioned
 582 above. Here are some key findings: (i) we were able to recreate the spacing and width
 583 of various Liesegang-like patterns based on the initial iron oxide distribution and water
 584 flow velocity; (ii) lower initial iron oxide concentration seems to favor the formation of
 585 slanted patterns, and the angle of the slant can reveal information about the rock's in-
 586 ternal structure; (iii) for straight, banded patterns, we identified a linear relationship be-
 587 tween the controlling factors and the thickness of the bands.

588 Our classification system allows us to match simulated patterns with those observed
 589 in the field. This "reverse analysis" helps us to estimate the key parameters that con-
 590 trol pattern formation in different Zebra rock locations. By comparing simulated pat-
 591 terns with real-world observations, we found a close resemblance, suggesting the model's
 592 accuracy. This paves the way for a powerful tool: a computer-aided interpretation frame-
 593 work. This tool can analyze patterns captured in field photographs, similar to Zebra rocks.
 594 We can then estimate crucial geochemical parameters that were present when the pat-

595 terns formed, including the chemical makeup and water flow conditions. The model's ca-
 596 pability to interpret past environments is particularly valuable for understanding the con-
 597 ditions on early Earth and Mars. By analyzing patterns in rocks from these locations,
 598 we can potentially uncover clues about the chemical conditions and fluid movement that
 599 existed billions of years ago.

600 6 Open Research

601 The Finite Element Method code and numerical results will be available after peer
 602 review.

603 Acknowledgments

604 The authors wish to acknowledge the generous support of the Western Australian Mu-
 605 seum for the supply of the high quality images of Zebra Rock in particular Geoff Dea-
 606 con for taking the photos and the curator Peter Downes for managing the request. The
 607 support of the Research Grant Council of Hong Kong (ECS 27203720 and GRF 17206521)
 608 and the Australian Research Council (ARC DP200102517, DP170104550, LP170100233)
 609 is acknowledged.

610 References

- 611 Al-Ghoul, M., & Sultan, R. (2019). Simulation of geochemical banding: Theoretical
 612 modeling and fractal structure in acidization-diffusion-precipitation dynamics.
 613 *Physical Review E*, *100*(5), 052214.
- 614 Antal, T., Droz, M., Magnin, J., & Rácz, Z. (1999). Formation of Liesegang pat-
 615 terns: A spinodal decomposition scenario. *Physical Review Letters*, *83*(15),
 616 2880.
- 617 Arndt, D., Bangerth, W., Blais, B., Clevenger, T. C., Fehling, M., Grayver, A. V.,
 618 ... Wells, D. (2020). The deal.II Library, Version 9.2. *Journal of Numerical*
 619 *Mathematics*, *28*(3), 131-146.
- 620 Arvidson, R., Squyres, S., Bell III, J., Catalano, J., Clark, B., Crumpler, L., ... oth-
 621 ers (2014). Ancient aqueous environments at Endeavour crater, Mars. *Science*,
 622 *343*(6169), 1248097.
- 623 Barge, L., Hammond, D., Chan, M., Potter, S., Petruska, J., & Nealon, K. (2011).
 624 Precipitation patterns formed by self-organizing processes in porous media.
 625 *Geofluids*, *11*(2), 124-133.
- 626 Cahn, J. W. (1961). On spinodal decomposition. *Acta Metallurgica*, *9*(9), 795-801.
- 627 Cahn, J. W., & Hilliard, J. E. (1958). Free Energy of a Nonuniform System. I. Inter-
 628 facial Free Energy. *The Journal of Chemical Physics*, *28*(2), 258-267.
- 629 Chan, M. A., Beitler, B., Parry, W., Ormö, J., & Komatsu, G. (2004). A possi-
 630 ble terrestrial analogue for haematite concretions on mars. *Nature*, *429*(6993),
 631 731-734.
- 632 Coward, A. J., Slim, A. C., Brugger, J., Wilson, S., Williams, T., Pillans, B., &
 633 Maksimenko, A. (2023). Mineralogy and geochemistry of pattern formation
 634 in zebra rock from the East Kimberley, Australia. *Chemical Geology*, *622*,
 635 121336.
- 636 DeWitt, S., Rudraraju, S., Montiel, D., Andrews, W. B., & Thornton, K. (2020).
 637 PRISMS-PF: A general framework for phase-field modeling with a matrix-free
 638 finite element method. *npj Computational Materials*, *6*(1), 1-12.
- 639 Foard, E., & Wagner, A. (2012). Survey of morphologies formed in the wake of an
 640 enslaved phase-separation front in two dimensions. *Physical Review E*, *85*(1),
 641 011501.
- 642 Furukawa, H. (1992). Phase separation by directional quenching and morphologi-
 643 cal transition. *Physica A: Statistical Mechanics and its Applications*, *180*(1-2),

- 644 128–155.
- 645 Geidans, L. (1981). Zebra rock of Western Australia. In *Geological Society of Aus-*
646 *tralia, Abstracts* (Vol. 3, p. 22).
- 647 Hu, M., Sun, Q., Schrank, C., & Regenauer-Lieb, K. (2022). Cross-scale dynamic
648 interactions in compacting porous media as a trigger to pattern formation. *Geo-*
649 *physical Journal International*, 230(2), 1280–1291.
- 650 Ishikawa, R., Tani, M., & Kurita, R. (2022). Three-dimensional phase separation
651 under a nonstationary temperature field. *Physical Review Research*, 4(3),
652 033152.
- 653 Kawahara, H., Yoshida, H., Yamamoto, K., Katsuta, N., Nishimoto, S., Umemura,
654 A., & Kuma, R. (2022). Hydrothermal formation of Fe-oxide bands in zebra
655 rocks from northern Western Australia. *Chemical Geology*, 590, 120699.
- 656 Krekhov, A. (2009). Formation of regular structures in the process of phase separa-
657 tion. *Physical Review E*, 79(3), 035302.
- 658 Larcombe, C. (1926). Some rocks from four miles east of Argyle Station, Ord River,
659 King district, Kimberley division. *Geological Survey of Western Australia, An-*
660 *ual Report*, 23.
- 661 L’Heureux, I. (2013). Self-organized rhythmic patterns in geochemical systems.
662 *Philosophical Transactions of the Royal Society A: Mathematical, Physical and*
663 *Engineering Sciences*, 371(2004), 20120356.
- 664 Liu, B., Zhang, H., & Yang, Y. (2000). Surface enrichment effect on the morphologi-
665 cal transitions induced by directional quenching for binary mixtures. *The Jour-*
666 *nal of Chemical Physics*, 113(2), 719–727.
- 667 Liu, C., Calo, V., Regenauer-Lieb, K., & Hu, M. (2023a). Coefficients of reaction-
668 diffusion processes derived from patterns in rocks. *Journal of Geophysical Re-*
669 *search: Solid Earth*, 128(5), e2022JB026253.
- 670 Liu, C., Calo, V. M., Regenauer-Lieb, K., & Hu, M. (2023b). Dendritic growth
671 patterns in rocks: Inverting the driving and triggering mechanisms. *Journal of*
672 *Geophysical Research: Solid Earth*, 128(9), e2023JB027105.
- 673 Liu, C., Hu, M., & Regenauer-Lieb, K. (2022). Liesegang Patterns Interpreted as a
674 Chemo-Hydromechanical Instability. In *Multiscale Processes of Instability, De-*
675 *formation and Fracturing in Geomaterials: Proceedings of 12th International*
676 *Workshop on Bifurcation and Degradation in Geomechanics* (pp. 59–66).
- 677 Loughnan, F., & Roberts, F. (1990). Composition and origin of the ‘zebra rock’ from
678 the East Kimberley region of Western Australia. *Australian Journal of Earth*
679 *Sciences*, 37(2), 201–205.
- 680 Mattievich, E., Chadwick, J., Cashion, J., Boas, J., Clark, M., & Mackie, R. (2003).
681 Macroscopic ferromagnetic liquid crystals determine the structure of Kimberley
682 zebra rock. In *Proceedings of the 27th Annual A&NZIP Condensed Matter and*
683 *Materials Meeting* (pp. 1–3).
- 684 Ortoleva, P. J., Merino, E., Moore, C., & Chadam, J. (1987). Geochemical self-
685 organization i; reaction-transport feedbacks and modeling approach. *American*
686 *Journal of Science*, 287(10), 979–1007.
- 687 Ostwald, W. (1902). *Lehrbuch der allgemeinen Chemie* (Vol. 2). W. Engelmann.
- 688 Qiu, W. J., Zhou, M.-F., & Williams-Jones, A. E. (2024). Numerical Simulation of
689 the Self-Organizational Origin of Concentrically Zoned Aggregates of Siderite
690 and Pyrite in Sediment-Hosted Massive Sulfide Deposits. *Journal of Geophys-*
691 *ical Research: Solid Earth*, 129(3), e2023JB028101.
- 692 Retallack, G. (2021). Zebra rock and other Ediacaran paleosols from Western Aus-
693 tralia. *Australian Journal of Earth Sciences*, 68(4), 532–556.
- 694 Sheldon, N. D., & Retallack, G. J. (2001). Equation for compaction of paleosols due
695 to burial. *Geology*, 29(3), 247–250.
- 696 Tsukada, T., & Kurita, R. (2020). Mechanism behind columnar pattern forma-
697 tion during directional quenching-induced phase separation. *Physical Review*
698 *Research*, 2(1), 013382.

- 699 Wang, Y., Chan, M. A., & Merino, E. (2015). Self-organized iron-oxide cementation
700 geometry as an indicator of paleo-flows. *Scientific Reports*, *5*(1), 1–15.
- 701 Wang, Y., Xu, H., Merino, E., & Konishi, H. (2009). Generation of banded iron
702 formations by internal dynamics and leaching of oceanic crust. *Nature Geo-*
703 *science*, *2*(11), 781–784.
- 704 Yatsuda, Y., Tsushima, K., Fang, Q., & Nabika, H. (2023). Chemical Model for
705 Pattern Formation in Rocks via Periodic Precipitation of Iron Oxide Minerals.
706 *ACS Earth and Space Chemistry*, *7*(10), 2042–2049.
- 707 Yoshida, H., Hasegawa, H., Katsuta, N., Maruyama, I., Sirono, S., Minami, M., . . .
708 others (2018). Fe-oxide concretions formed by interacting carbonate and acidic
709 waters on Earth and Mars. *Science Advances*, *4*(12), eaau0872.
- 710 Yoshida, H., Katsuta, N., Sirono, S.-i., Nishimoto, S., Kawahara, H., & Metcalfe, R.
711 (2020). Concentric Fe-oxyhydroxide bands in dacite cobbles: Rates of buffering
712 chemical reactions. *Chemical Geology*, *552*, 119786.

Abstract

Zebra rocks, characterized by their striking reddish-brown stripes, rods, and spots of hematite (Fe-oxide), showcase complex self-organized patterns formed under far-from-equilibrium conditions. Despite their recognition, the underlying mechanisms remain elusive. We introduce a novel advection-dominated phase-field model that effectively replicates the Liesegang-like patterns observed in Zebra rocks. This model leverages the concept of phase separation, a well-established principle governing Liesegang phenomena. Our findings reveal that initial solute concentration and fluid flow velocity are critical determinants in pattern selection and transition. We quantitatively explain the spacing and width of a specific Liesegang-like pattern category. Furthermore, the model demonstrates that vanishingly low initial concentrations promote the formation of oblique patterns, with inclination angles influenced by rock heterogeneity. Additionally, we establish a quantitative relationship between band thickness and geological parameters for orthogonal bands. This enables the characterization of critical geological parameters based solely on static patterns observed in Zebra rocks, providing valuable insights into their formation environments. The diverse patterns in Zebra rocks share similarities with morphologies observed on early Earth and Mars, such as banded iron formations and hematite spherules. Our model, therefore, offers a plausible explanation for the formation mechanisms of these patterns and presents a powerful tool for deciphering the geochemical environments of their origin.

Plain Language Summary

Zebra rocks, known for their unique red and brown stripes and spots, hold clues to how similar patterns formed on early Earth and Mars. We have developed a new model to explain how these intriguing patterns form. The model suggests that the flow of fluids and the initial amount and location of dissolved iron-oxide (rust) in water plays a big role in shaping the final Zebra rock design. The speed of the flow and the initial amount of rust can create different stripe and spot patterns, just like the ones in Zebra rocks. By studying these rocks, we can potentially decipher fluid flow scenarios of ancient environments on both Earth and Mars.

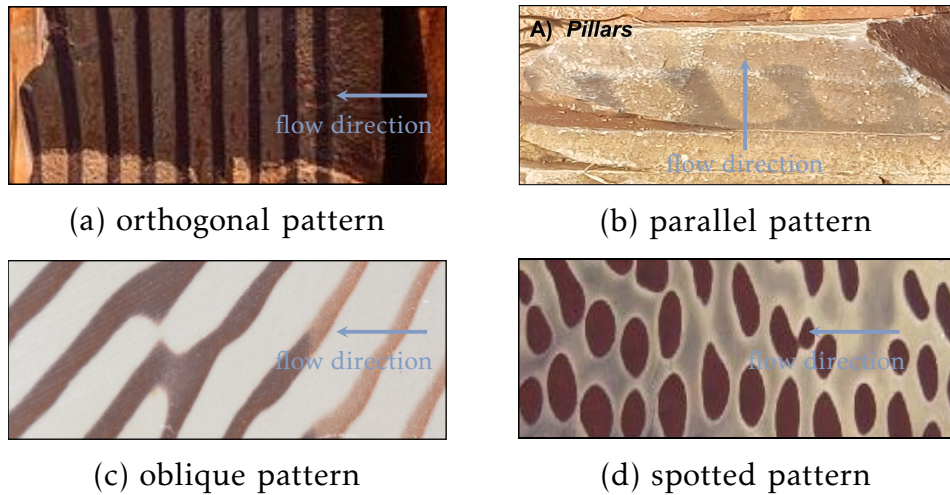
1 Introduction

When geological systems are far from equilibrium, self-organization processes can form geochemical patterns autonomously (Ortoleva et al., 1987; L’Heureux, 2013; Wang et al., 2015; Al-Ghoul & Sultan, 2019; C. Liu et al., 2022, 2023a; Yatsuda et al., 2023; Qiu et al., 2024). Heterogeneity of geological materials and systems as well as complicated boundary conditions can make the observed patterns rich in information about the geological environments in which they are formed, particularly concerning fluid migration and initial conditions. In this contribution we develop a theory and method to use these patterns to provide a window into the past of planetary evolution.

One example of extensively studied pattern formation is the formation of variable hematite (Fe-oxide) on early Earth and Mars, including the Zebra rock formation, Precambrian banded iron formations (BIFs), Mississippi-Valley-type (MVT) ores, and others (Wang et al., 2009, 2015; C. Liu et al., 2023a). Field evidence suggests that groundwater flows influence the formation of Fe-oxide precipitation bands and that BIFs may reflect the changing composition of the oceanic crust (Kawahara et al., 2022; Wang et al., 2009). Additionally, concretions formed in Jurassic Navajo Sandstone have been proposed as a terrestrial analog to hematite spherules detected by the rover Opportunity at the Meridiani Planum site on Mars (Chan et al., 2004; Arvidson et al., 2014; Yoshida et al., 2018). Therefore, a better understanding of the pattern-forming processes in rocks and minerals can reveal valuable information about the geological environment on early

64 Earth and Mars, including the possibility of aqueous environments on Mars and the abil-
 65 ity to invert fluid flow velocity and initial solute concentration on early Earth.

66 We study the Zebra Rock pattern in the northern region of Western Australia, which
 67 exhibits a unique and highly noticeable rhythmic concentration of hematite (Kawahara
 68 et al., 2022). Among all hematite banding patterns, none are as distinct and rich as the
 69 Zebra rock patterns. Thus, the Zebra rock formation is an excellent analog for various
 70 pattern-forming processes associated with subsurface environmental evolution. Zebra rock
 71 formation contains reddish-brown bands, rods, and elliptical spots on a white or light-
 72 colored background, as shown in Figure 1. In our earlier work, we linked Zebra rock for-
 73 mation to the Liesegang phenomenon, a process where supersaturation, nucleation (for-
 74 mation of solid particles), and depletion compete to create banded patterns (C. Liu et
 75 al., 2023a, 2023b). This connection was made because some Zebra rock patterns look sim-
 76 ilar to Liesegang bands. However, classic Liesegang bands typically show increasing band
 77 thickness and spacing as they form. Zebra rocks, on the other hand, exhibit a wider var-
 78 iety of patterns. To differentiate these, we refer to the Zebra rock patterns as Liesegang-
 79 like patterns throughout this study.



80 **Figure 1.** Rich patterns appear in Zebra rocks in the northern region of Western Australia:
 81 (a) orthogonal pattern; (b) parallel pattern (after Coward et al. (2023)); (c) oblique pattern; and
 82 (d) spotted patterns.

83 The fundamental Liesegang precipitation model helps to explain the forming mech-
 84 anism of Zebra rocks (Loughnan & Roberts, 1990; Kawahara et al., 2022; Coward et al.,
 85 2023; C. Liu et al., 2023a). However, there are many other hypotheses regarding their
 86 origin, including alternating sedimentation either in marine environments (Larcombe,
 87 1926) or ripple trough (Geidans, 1981), ferronematic liquid crystals (Mattievich et al.,
 88 2003), acid-sulfate soil weathering in conjunction with redox (Retallack, 2021).

89 Recently, acidic-hydrothermal alterations have been suggested to form Liesegang-
 90 like patterns behind a moving front of concentrated iron (Kawahara et al., 2022). How-
 91 ever, this theory faces several challenges in explaining the diverse Zebra rock patterns:
 92 (i) the Liesegang theory predicts only simple band or ring patterns, while Zebra rocks
 93 exhibit a wider variety, including horizontal, vertical, and slanted stripes; (ii) diffusion-
 94 driven Liesegang patterns typically form over a small area. The theory has difficulties
 95 in explaining the vast, multi-layered patterns observed in the Ediacaran Ranford For-
 96 mation, spanning over 45 kilometers (Coward et al., 2023); (iii) the Liesegang model is

97 limited in explaining pattern shape variations and cannot generate the spotted or rod-
98 shaped patterns commonly seen in Zebra rock formations (Coward et al., 2023).

99 In an earlier contribution, we aimed to overcome some limitations of the Liesegang
100 model, using the Cahn-Hilliard model to describe the mineral precipitation in a phase
101 separation model in binary mixtures (C. Liu et al., 2023a). In this case, stripe patterns
102 with the externally imposed periodicity can be stabilized against coarsening above some
103 critical modulation amplitude. However, two essential questions were raised by this model.
104 First, the diffusion-dominated model may not produce the vast Zebra rocks formation
105 argued by Wang et al. (2015). Fluid transport should be necessary for this giant Zebra
106 rock to form across several kilometers horizontally. Second, while the previous model can
107 produce banded and spotted patterns when varying diffusion coefficient or solute mo-
108 bility, it cannot generate the variable bands photographed in the field, containing hor-
109 izontal, oblique, and vertical stripes. Thus, we investigate whether directional quench-
110 ing can create the observed Liesegang-like patterns. This transport-limited model con-
111 centrates on the phase separation process by neglecting the diffusion of the reactants and
112 focusing on the dominant fluid flow. Consequently, we investigate whether the fluid trans-
113 port velocity and initial conditions uniquely determine the pattern morphology.

114 The phase separation process with advection, where fluid flow transports different
115 components, can generate a wide variety of self-organized patterns in various systems.
116 These include binary alloys, fluid mixtures, polymer blends, and even nanostructured
117 thin films. In material science, controlling this process is crucial for designing nanoma-
118 terials and nanodevices with specific functionalities. For example, researchers can cre-
119 ate regular structures desirable for applications ranging from bioactive implants to poly-
120 mer electronics. In such studies Furukawa (1992) investigated the transition between dif-
121 ferent morphologies (shapes) in a binary mixture by varying the speed of the quench-
122 ing front, the boundary between the separated phases. They observed and classified three
123 main categories: irregular, regular lamellar (layered), and regular columnar morpholo-
124 gies. Since then, researchers have introduced alternative descriptions for these transi-
125 tions, considering factors like dimensionality (2D vs. 3D) (Ishikawa et al., 2022), bound-
126 ary and temperature effects (B. Liu et al., 2000; Ishikawa et al., 2022), and the under-
127 lying mechanisms governing the transitions (Krekhov, 2009; Tsukada & Kurita, 2020).

128 In this contribution we extend the analysis to decipher the geological environments
129 by interpreting geological patterns, particularly pattern formation in Zebra rocks. Al-
130 though the advection-dominated phase separation model is successfully applied in ma-
131 terial science, there are still several research gaps in adopting it in geological pattern for-
132 mation: (i) the mechanism of oblique patterns, one of the most notable patterns, remains
133 unclear; (ii) the morphological transition from one particular pattern to the oblique pat-
134 tern is unexplained; (iii) Liesegang patterns are not replicated by the advection-dominated
135 phase separation even though it commonly occurs in diffusion-dominated formulations;
136 (iv) the association between the migration velocities and the band thickness of the uni-
137 form patterns remains unclear; (v) the plausibility of deriving geological environments
138 by reproducing the pattern appearance in Zebra rocks needs investigation. We seek to
139 fill these research gaps by adopting the working hypothesis of Kawahara et al. (2022) and
140 studying the phase separation of Fe-oxyhydroxide under acidic Fe-bearing fluid trans-
141 port conditions by performing numerical simulations in a two-dimensional setting. Note
142 that the model is not limited to the choice of the specific phase separation reaction. How-
143 ever, if a reaction can be identified, the normalized velocities and concentrations can be
144 quantified further by comparing them to laboratory results of the particular reaction cho-
145 sen. We focus here primarily on the investigation of the effect of the transport velocity
146 and initial Fe-oxyhydroxide concentration on the pattern selection and transitions.

147 The remaining parts of this study are organized as follows. Section 2 presents the
148 Cahn-Hilliard formulation with the convection term, which can capture the phase sep-
149 aration process during mineral precipitation. In Section 3, we first select numerical pa-

150 rameters through a series of convergence studies, and then we conduct parameter stud-
 151 ies regarding the transport velocity and initial Fe-oxyhydroxide concentration to inves-
 152 tigate the pattern selection and transition, especially detailed studies for three different
 153 banded patterns. Eventually, we invert the potential geological pattern by replicating
 154 the field patterns photographed in a few Zebra rock outcrops. Section 4 discusses our
 155 numerical results and suggests potential applications of our model in the future. Finally,
 156 we conclude our study in Section 5.

157 2 Methodology

158 2.1 Cahn-Hilliard model

We adopt a classical Cahn-Hilliard model to study Liesegang-like pattern forma-
 tion in a reaction-advection-diffusion system $A_{(aq)} + B_{(aq)} \rightarrow C_{(s)}$. In our study, two
 reagents A and B denoting Fe-bearing acidic fluid and dolomite, respectively, in our study,
 react and produce C (i.e., Fe-oxyhydroxide). This model captures the phase separation
 dynamics occurring in the wake of the fluid front with the $A+B$ chemical reaction. We
 focus on pattern formation and transition by simulating the dynamics of the phase-separating
 chemical C in our model instead of including its production as we studied in our pre-
 vious model (C. Liu et al., 2023a). Using this model, the reaction product C can be sep-
 arated into low- and high-concentration phases (Antal et al., 1999). The concentration
 contrast between phases leads to the forming of precipitation patterns. In this study, the
 Fe-oxyhydroxide concentration enters an unstable region (a.k.a. spinodal), where it di-
 vides into a low-concentration region (no precipitate) and a high-concentration region
 (precipitate), which is underpinned by the classical Cahn-Hilliard equation (Cahn & Hilliard,
 1958; Cahn, 1961):

$$\frac{\partial c}{\partial t} = -\nabla \cdot \left(\lambda \nabla \frac{\delta F}{\delta c} \right) \quad (1)$$

where c is the concentration of the reaction product C and λ is the diffusive mobility;
 we assign $\lambda = 1$ in current study. Let $\mu = \delta F / \delta c = I'_c + B'_c$ be a generalized thermo-
 dynamic potential that drives the phase separation. The interfacial energy is

$$I_c = \frac{1}{2} \sigma |\nabla c|^2 \quad (2)$$

165 in which σ is a constant relevant to interface sharpness; we set it to $\sigma = 0.5$.

In addition, again for simplicity, we use a Landau-Ginzburg type free energy den-
 sity with two minima corresponding to c_l and c_h and the maximum to $\bar{c} = (c_l + c_h)/2$.

$$B_c = \frac{\varepsilon}{2} (c - \bar{c})^2 - \frac{\gamma}{4} (c - \bar{c})^4 \quad (3)$$

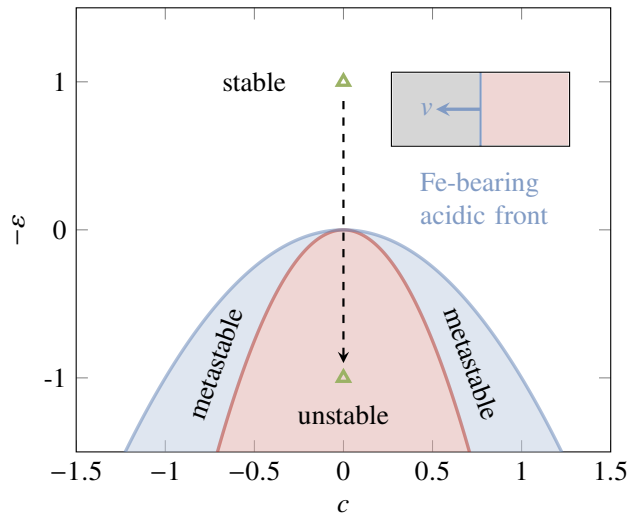
where ε and γ are system-dependent parameters. Here, we assume $\gamma = 1$ and vary the
 parameter ε to control the phase separation process. When $\varepsilon < 0$, the system is sta-
 ble with a single minimum; when $\varepsilon > 0$, the system experiences phase separation with
 two minima. We simply mimic the transport of the Fe-bearing acidic front by varying
 the parameter ε . Initially, we set $\varepsilon = -1$ in the whole system as the static state before
 the Fe-bearing acidic front reaches. During the reactive transport process, the param-
 eter ε varies over both time and space as follows:

$$\varepsilon = \begin{cases} -1, & \text{if } x < vt \\ 1, & \text{if } x \geq vt \end{cases} \quad (4)$$

166 where v is a constant velocity denoting the transport of the Fe-bearing acidic fluid front
 167 and t is time.

Finally, by substituting the chemical potential equations (2) and (3), the Cahn-Hilliard
 equation (1) becomes

$$\frac{\partial c}{\partial t} = \nabla \cdot (\lambda \nabla (-\varepsilon c + \gamma c^3 - \sigma \Delta c)) \quad (5)$$



159 **Figure 2.** Qualitative phase diagram for the phase separation. Phase separation takes place
 160 when $\varepsilon > 0$. The system becomes unstable as $|c| < 1/\sqrt{3}$, while the system is metastable when
 161 $|c| > 1/\sqrt{3}$. The system initially has a negative $\varepsilon = -1$, but the concentration is in the unstable
 162 region. After the Fe-bearing acidic fluid sweeps at constant speed v , we switch $\varepsilon = -1$ to $\varepsilon = 1$.
 163 By doing this, the fluid-swept area will experience phase separation, and different patterns will
 164 emerge. Adapted from Tsukada and Kurita (2020).

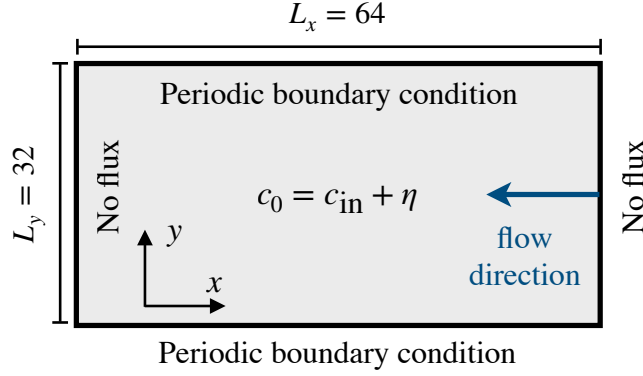
We use a mixed discretization of the system where we avoid the fourth term in the equation (5) by considering the chemical potential μ as an auxiliary variable to facilitate using the standard bilinear finite element space. Then the governing equation (5) separates as

$$\begin{aligned} \frac{\partial c}{\partial t} &= \nabla \cdot (\lambda \nabla \mu) \\ \mu &= -\varepsilon c + \gamma c^3 - \sigma \Delta c \end{aligned} \quad (6)$$

168 2.2 Problem statement

171 We consider an initial-boundary value problem in a rectangular domain Ω as displayed in Figure 3. The domain size is $L_x = 64$ in height and $L_y = 32$ in width, sufficiently large to present different categories of patterns. We impose periodic boundary conditions on the top and bottom edges for both concentration and chemical potential and use the natural boundary condition on the lateral edges. Initially, the product C concentration is set to the stable magnitude, $c_0 = c_{\text{in}} + \eta$ in the whole region, where η denotes noise effects, such as the heterogeneous reagents and thermal fluctuations. We assume η as a random distribution in the range $[-0.01, 0.01]$, a typical value for homogeneous phase-separation simulations (Foard & Wagner, 2012). We put the position of the Fe-bearing acidic fluid front at $x = L_x$. As a result, the whole domain initially remains stable. After the front moves left, the swept region undergoes spinodal decomposition, creating a phase-separating pattern.

183 After determining the boundary and initial conditions, the governing equations (6)
 184 can be solved by PRISMS-PF (DeWitt et al., 2020), which is an open-source, high-performance
 185 phase-field code built on a finite element library `deal.ii` (Arndt et al., 2020). Interested
 186 readers can derive the weak form based on the Cahn-Hilliard implication. In addition,
 187 we use the forward Euler method as the time marching technique. To this end, we should



169 **Figure 3.** Sketch of initial and boundary conditions for Liesegang-like patterns formation
 170 after the infiltration of Fe-bearing fluid flow.

188 select the time increment satisfying the Courant–Friedrichs–Lewy (CFL) condition, which
 189 has been implemented in PRISMS-PF.

190 3 Results

191 We use the Cahn–Hilliard model described in Section 2 to numerically study the
 192 phase separation phenomenon observed in a geological setting. First, we conduct con-
 193 vergence studies in space and time to choose an appropriate mesh size and time incre-
 194 ment in Section 3.1. After selecting the suitable numerical parameters, in Section 3.2,
 195 we perform parameter studies on the speed of the Fe-bearing acidic fluid front as well
 196 as the initial concentration of the product, which plays a decisive role in selecting the
 197 morphology appearance. Finally, Section 3.3 reproduces the different patterns observed
 198 in Zebra rocks by the numerical simulations.

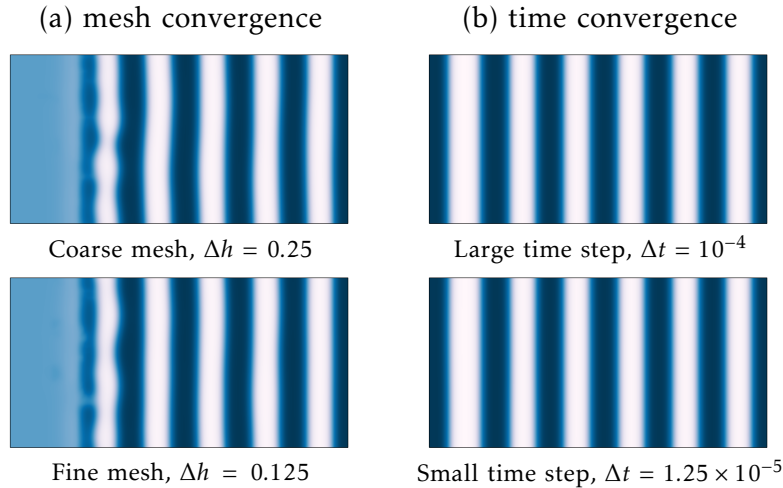
199 3.1 Model convergence study

203 We demonstrate PRISMS-PF’s capability for simulating phase separation problems
 204 by conducting convergence studies in space and time. We perform two simulations for
 205 the mesh size h selection with a fixed time increment $\Delta t = 1.25 \times 10^{-5}$. We vary the
 206 mesh size as $\Delta h = 0.125$ and $\Delta h = 0.25$, respectively. The selections ensure the typi-
 207 cal value, i.e., $\sigma/\Delta h$ ranging from 2 to 4, for the phase field methods capturing the struc-
 208 ture and interfacial evolution. Figure 4a shows that the resulting patterns are similar
 209 except for the localized noise emerging in the transport front. This is because the noise
 210 term is introduced in the initial concentration distribution. Meanwhile, the band loca-
 211 tions match well, demonstrating the noise cannot change the internal characteristics.

212 Additionally, we select the appropriate time step size by performing the temporal
 213 convergence. We fix the mesh size as $\Delta h = 0.25$ but vary the time size as $\Delta t = 10^{-4}$
 214 and $\Delta t = 1.25 \times 10^{-5}$, respectively. The pattern formation after the transport front
 215 approaches the left boundary is depicted in Figure 4b. The reduced time step is in ex-
 216 cellent agreement with the large time step. These results imply that the time size $\Delta t =$
 217 10^{-4} is small enough to guarantee converged results.

218 3.2 Parameter space analysis and patterning

219 We thoroughly explore the parameter spaces to understand better how parameters
 220 affect the pattern formation and transition as the Fe-bearing fluid passes one geologi-
 221 cal formation. We identify the two main parameters responsible for pattern formation



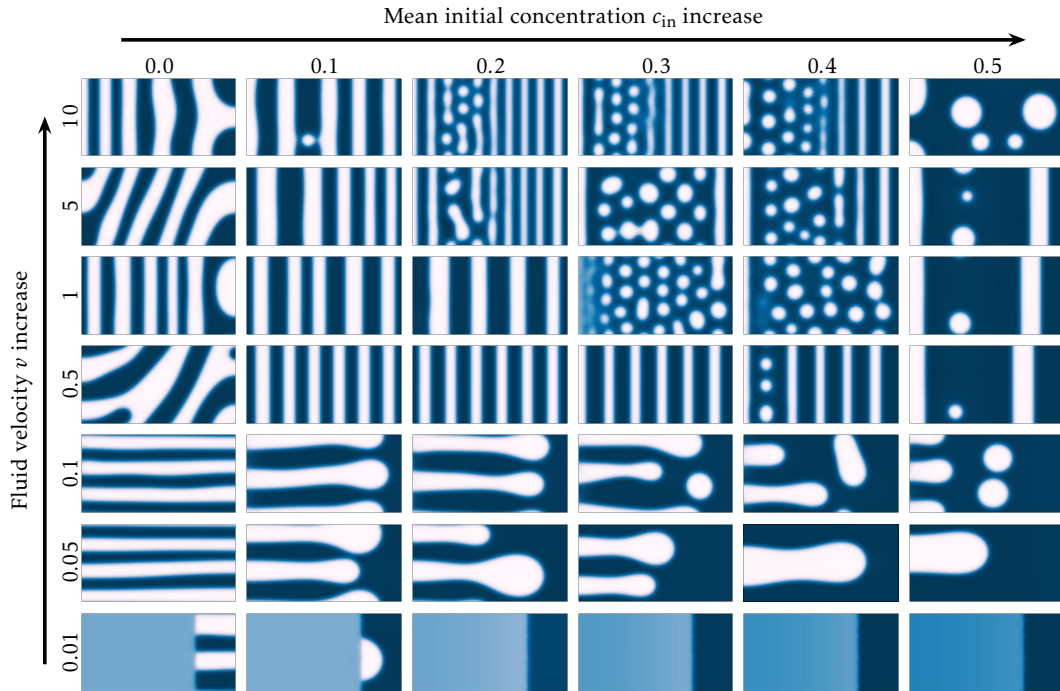
200 **Figure 4.** Convergence studies determining numerical parameters: (a) mesh size and (b) in-
 201 cremental time step. Parameters used in these simulations are $\lambda=1$, $\sigma=0.5$, $\gamma=1$, and ε shifting
 202 from -1 to 1 after the fluid front passes.

222 and selection: the fluid velocity v and initial solute concentration c_{in} . We create a phase
 223 morphology diagram that illustrates the various patterns by fixing one control param-
 224 eter constant while adjusting another. From our simulation results, we initially classify
 225 these patterns into five morphologies by their characteristics and the formed pattern with
 226 the direction of the fluid flow. Subsequently, we assess one category of banded patterns
 227 quantitatively by relating the spacing coefficient with the fluid speed. These simulations
 228 use the same setup as those described in Section 3.1.

229 3.2.1 Morphology phase diagram

235 We numerically examine how the fluid velocity v and initial solute concentration
 236 c_{in} influence the pattern evolution. For the parameter sweep, we consider seven differ-
 237 ent fluid velocities, spanning several orders of magnitude from 0.001 to 10, to ensure the
 238 emergence of all potential morphologies. Additionally, we set the initial solute concen-
 239 tration c_{in} from 0.0 to 0.5 with an increment of 0.1, satisfying the spinodal decomposi-
 240 tion condition with a limit of $c_{\text{in}} < 1/\sqrt{3}$ in Figure 2. As a result, we perform 42 simu-
 241 lations to observe the morphology evolution while varying v and c_{in} , as shown in Fig-
 242 ure 5. It is worth noting that we end each simulation as long as the corresponding pat-
 243 tern shows all the characteristics.

244 First, we classify the patterns that emerge following the phase separation, as the
 245 resulting patterns exhibit great versatility. Drawing upon the features exhibited by these
 246 patterns, we categorize them as banded or spotted patterns, as discussed in our recent
 247 work (C. Liu et al., 2022, 2023a). To avoid any potential confusion, we refer to patterns
 248 with a spotty appearance as spotted patterns. Furthermore, within the banded morpholo-
 249 gies, we further classify them into three distinct categories based on the direction of the
 250 bands relative to the fluid flow: (i) orthogonal bands, characterized by stripes perpen-
 251 dicular to the fluid flow direction; (ii) parallel bands, oriented in parallel with the fluid
 252 front; and (iii) oblique bands, displaying an inclined angle relative to the fluid front. No-
 253 tably, no discernible pattern is observed in some instances referred to as homogeneous
 254 cases. In total, our simulations yield five distinct pattern types. Although this simple
 255 classification of morphologies is based on our numerical findings, it provides a valuable
 256 tool for visually distinguishing patterns observed in geological settings on Earth and Mars (Barge

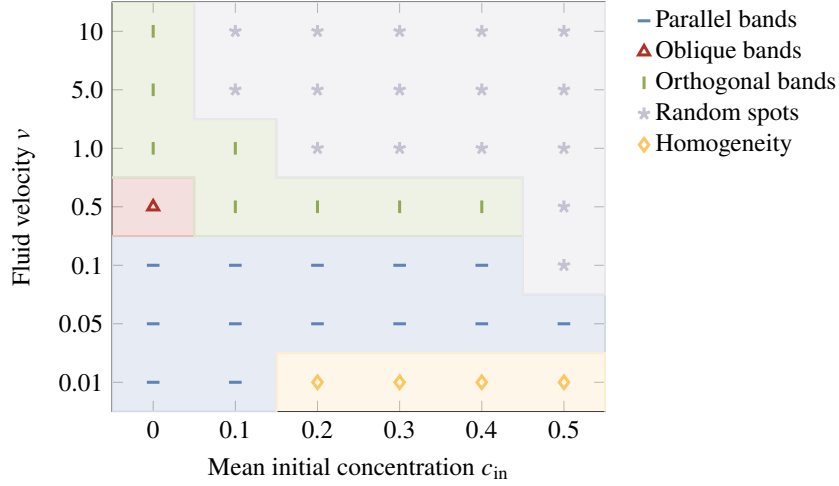


230 **Figure 5.** Morphology evolution in the phase diagram where the initial solute concentration
 231 and fluid front speed are varied.

257 et al., 2011; Wang et al., 2015; Yoshida et al., 2018). An example is the patterns observed
 258 in Zebra rocks (Coward et al., 2023). According to the proposed classification criterion,
 259 we divide the generated patterns into five groups. Figure 6 shows that the fluid velocity
 260 v and initial solute concentration c_{in} are crucial to determining the pattern type.

261 Second, we investigate the effect of the Fe-bearing fluid velocity on the pattern forma-
 262 tion and transition as we can observe the simulated patterns from the bottom to top
 263 in Figure 6, the simulated patterns transition from parallel bands to orthogonal bands
 264 and ultimately to spotted patterns. This transition depends on the initial concentration
 265 level c_{in} . The transition speed from the striped to spotted patterns is particularly sen-
 266 sitive to concentration, with the speed decreasing as c_{in} increases. In contrast, when $c_{in} <$
 267 0.5 , the transition speed from parallel to orthogonal stripes is gentler and remains con-
 268 stant throughout our simulations. Without refined simulations conducted, we report the
 269 trend that the transition velocity tends to decrease between 0.1 and 0.5 as c_{in} increases.
 270 This phenomenon becomes apparent when c_{in} reaches 0.5 , and the front velocity v drops
 271 from 0.1 to 0.05 . Furthermore, homogeneity only arises when the slow velocity is com-
 272 bined with a relatively high initial concentration. Interestingly, oblique bands are only
 273 observed once in our phase diagram, with $c_{in} = 0$ and $v = 0.5$. Given the uniqueness
 274 of this pattern, we provide an in-depth analysis in the following section.

275 Finally, we survey the pattern evolution in the horizontal axis to test the influence
 276 of the initial concentration c_{in} . Unlike the comprehensive spectrum of transitions observed
 277 when varying the Fe-bearing fluid velocity, changing the concentration c_{in} with a fixed
 278 v results in only one discernible transition. However, an exception occurs when $v = 0.5$,
 279 where oblique stripes appear when $c_{in} = 0$. When the transport velocity v is relatively
 280 low, pure parallel patterns emerge, while a transition from orthogonal bands to spots is



232 **Figure 6.** Morphology classification based on the pattern features: homogeneous, banded, and
 233 spotted patterns and the banded patterns relative to the fluid direction: parallel, oblique, and
 234 orthogonal patterns.

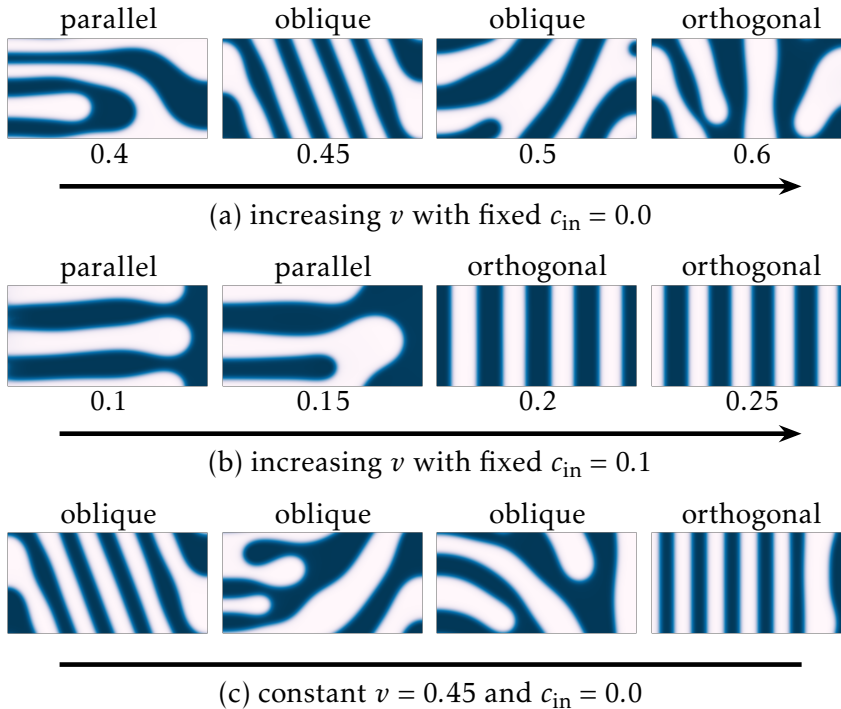
281 observed at higher velocities. Additionally, either parallel or orthogonal bands evolve into
 282 spot morphologies, but a transition between parallel and orthogonal stripes is absent.

283 3.2.2 Oblique band appearance

287 Oblique bands appear in a narrow area with the initial solution concentration $c_{in} =$
 288 0 in the morphology phase diagram. Figure 5 illustrates how the stripe patterns change
 289 from parallel to inclined and ultimately to orthogonal bands when the front speed ac-
 290 celerates from 0.1 to 1.0 with a fixed $c_{in} = 0$. We investigate the transition process by
 291 performing extra simulations with v ranging from 0.4 to 0.6 as Figure 7a shows. There,
 292 oblique patterns emerge at $v = 0.45$ and $v = 0.5$ but with different inclined directions
 293 relative to the fluid front.

294 The arbitrary occurrence of oblique bands is two-fold. First, the creation of the in-
 295 clined patterns depends on the competition between the emergence of parallel and or-
 296 thogonal bands. When the transport velocity reaches a critical value, the competition
 297 becomes comparable. As a consequence, the inclined pattern should appear. Second, this
 298 competitive mechanism explains the varied angles observed in the phase separation pro-
 299 cess occurring in an inhomogeneous system. The heterogeneity is realized by the noise
 300 term that we add in the initial condition. Figure 7c shows that the noise term can dra-
 301 matically affect the morphology selection. In these simulations, the randomly distributed
 302 noise term is the only changing parameter since we maintain the front velocity $v = 0.45$
 303 constant and vanish the initial concentration. Oblique bands with different directions
 304 can appear, even in the form of orthogonal patterns.

305 The initial solution concentration inhibits the occurrence of oblique patterns. As
 306 for the cases of $c_{in} = 0$, we understand that the oblique patterns develop between the
 307 parallel and orthogonal patterns. To test the possibility of inclined patterns when $c_{in} \neq$
 308 0, we capture the transition process from parallel bands to orthogonal bands as nonzero
 309 initial concentrations, e.g., $c_{in} = 0.1$, as Figure 7b shows. Numerical results show that
 310 oblique patterns cannot appear when parallel bands shift to orthogonal bands. The pat-
 311 tern features remain unaltered when we use the same setup as in the convergence stud-



284 **Figure 7.** Pattern formation and selection with increasing front speeds and fixed initial solute
 285 concentration: (a) $c_{in}=0$ and (b) $c_{in}=0.1$. (c) Constant front speed $c_{in}=0.45$ and concentration
 286 $c_{in}=0.0$ with different .

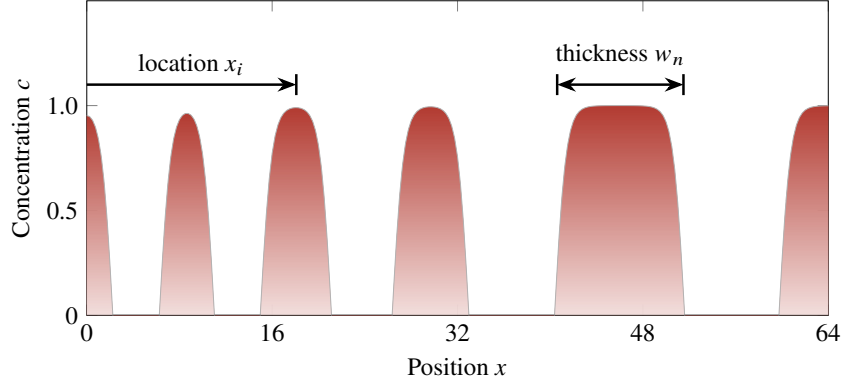
312 ies in Section 3.1. This implies that it is the initial concentration that controls the phase
 313 separation rather than the additional noise term.

314 Overall, the vanishing solute concentration plays a pivotal role in determining the
 315 appearance of oblique patterns, while the noise effect makes the oblique direction emerge
 316 arbitrarily. Our findings explain why randomly oblique patterns can develop in Zebra
 317 rocks in the same geological setting (Coward et al., 2023). Specifically, our study sug-
 318 gests that unprecipitated rocks with heterogeneity tend to develop oblique patterns.

319 **3.2.3 Orthogonal patterns with Liesegang phenomenon**

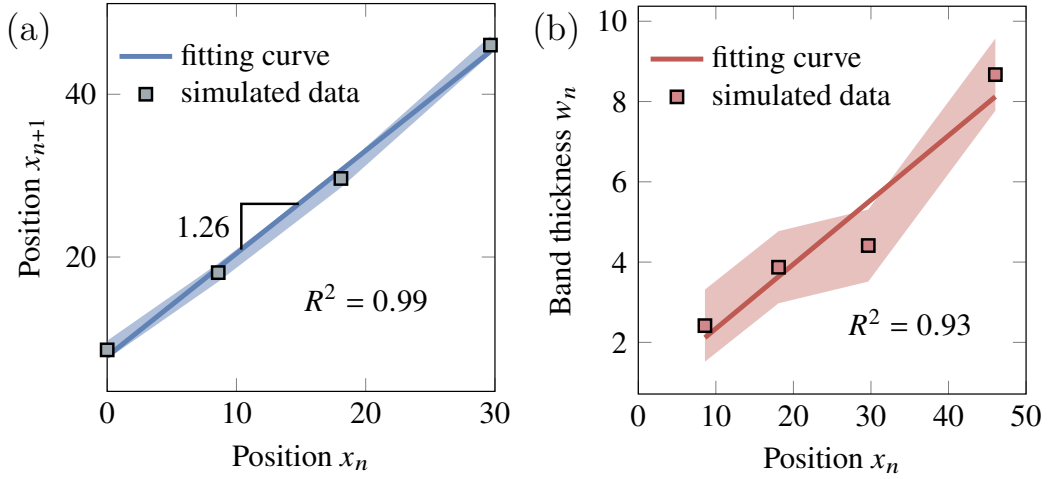
320 In the phase diagram, several orthogonal patterns exhibit characteristics reminis-
 321 cent of the Liesegang phenomenon. As observed in experiments, Liesegang bands are typ-
 322 ically governed by empirical laws regarding their formation time, locations, and widths.
 323 The time law cannot apply in our advection-dominated model since the empirical rela-
 324 tionships are built in the diffusion-limited experiments. However, we seek to quantita-
 325 tively validate the Liesegang-like patterns regarding spacing and width laws by focussing
 326 on a specific combination of $v = 5$ and $c_{in} = 0.1$ in Figure 5. This choice is made based
 327 on the fact that the simulated patterns exhibit behavior closely resembling Liesegang bands.

333 Figure 8 presents the product concentration distribution c along the x -axis follow-
 334 ing the passage of Fe-bearing fluid. As the fluid front propagates, rhythmic precipita-
 335 tion bands appear, forming regular Liesegang band patterns. Qualitatively, the width
 336 of periodic stripes and interband spacing increases, consistent with the behavior of Liesegang
 337 stripes. We quantitatively verify the empirical laws by measuring the band location, e.g.,
 338 i -th band location denoted by x_i , and band thickness, e.g., n -th band thickness repre-



328 **Figure 8.** The product concentration distribution c along the x -axis after the fluid flow, form-
 329 ing the regular Liesegang band patterns. x_i and w_n denote location and thickness of the i -th
 330 and n -th bands, respectively.

339 sented by and w_n . The location x_i represents the distance between the band center and
 the model boundary.



331 **Figure 9.** Verification of Liesegang bands: (a) spacing law and (b) width law. The shaded
 332 regions are the liner regression's root mean square error (RMSE).

340

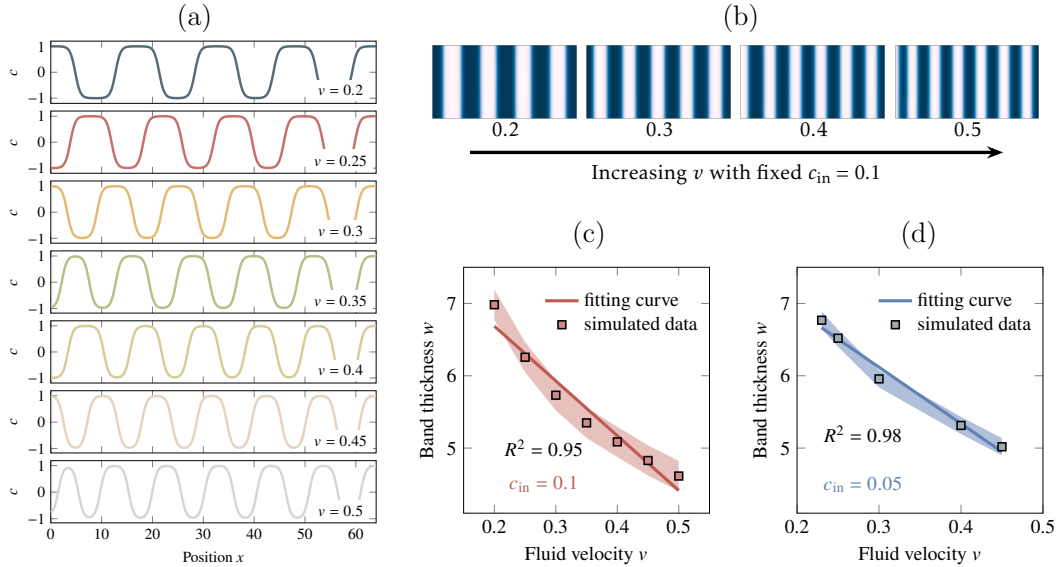
341 We provide quantitative validation for the selected bands and examine the behav-
 342 ior of Liesegang striping in terms of the empirical spacing and width laws. The spacing
 343 law indicates a linear relationship between the locations of subsequent bands, given by
 344 $x_{n+1}/x_n = 1 + p$, where $1 + p$ represents the spacing coefficient. Figure 9a shows this
 345 linear relationship, with a high coefficient of determination $R^2 = 0.99$. The estimated
 346 value of $1+p$ is approximately 1.26, falling within the 1 to 7 range, consistent with the
 347 inversion of Zebra rock samples from the same region (C. Liu et al., 2023a).

348 Additionally, we investigate the width law, which states that the bandwidth w_n is
 349 proportional to the position x_n of the band, i.e., $x_n \propto w_n$. Once again, Figure 9b shows
 350 a linear relation between x_n and w_n . By successfully reproducing these two empirical

351 observations from the Liesegang phenomenon, our simplified model demonstrates the abil-
 352 ity to replicate Liesegang patterns without considering the diffusion of reactants in the
 353 reaction-diffusion system.

354 3.2.4 Uniform pattern

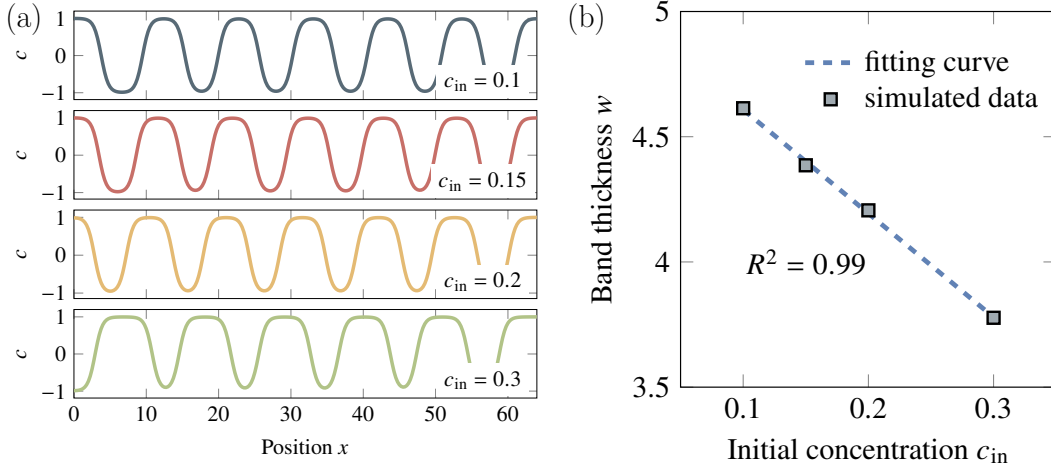
355 The uniform pattern, commonly observed in Zebra rocks, suggests that the spac-
 356 ing coefficient is around $1 + p \approx 1$, following the classical Turing pattern (Hu et al.,
 357 2022). This study’s uniform pattern refers to orthogonal bands exhibiting minimal strip
 358 variations. Through our simulations, we discover that the diffusion velocity and the initial
 359 concentration influence the bandwidth of each uniform pattern.



355 **Figure 10.** (a) The concentration profiles along the x -axis for varying transport velocities v ,
 356 ranging from 0.2 to 0.5 with a 0.05 increment, while maintaining a constant initial concentration
 357 of $c_{in}=0.1$. (b) The formation of uniform bands at the end of the simulation for four transport
 358 velocities. (c) and (d) The banded thickness measured from the simulations for initial concentra-
 359 tions $c_{in}=0.1$ and $c_{in}=0.05$, respectively, along with the corresponding linear fit.

364

368 We seek to gain a deeper understanding of the relationship between fluid speed and
 369 band thickness; thus, we conduct refined simulations in the phase diagram, varying the
 370 fluid speed v from 0.2 to 0.5 with 0.05 increments while maintaining a constant
 371 initial concentration of $c_{in} = 0.1$. Figure 10a shows the concentration profiles along the x -axis,
 372 where the bands are located in regions with $c > 0$. Figure 10b illustrates the forma-
 373 tion of regular patterns at four different velocities. The repeated bands exhibit nearly
 374 identical thickness w_n in each simulation. Therefore, we calculate the average band thick-
 375 ness to assess the generated thickness for different front velocities. Subsequently, we plot
 376 the band thickness against the corresponding velocity in Figure 10c. Our results indi-
 377 cate that the band thickness is proportional to the fluid front speed. Specifically, a higher
 378 front speed v leads to a decrease in the band thickness w_n , consistent with the finding
 379 from Yoshida et al. (2020). We conduct five additional simulations for $c_{in} = 0.05$ to val-
 380 idate this linear relationship further. In analogy to the case of $c_{in} = 0.1$, the simula-
 381 tions exhibit the same linear trend as Figure 10d depicts.



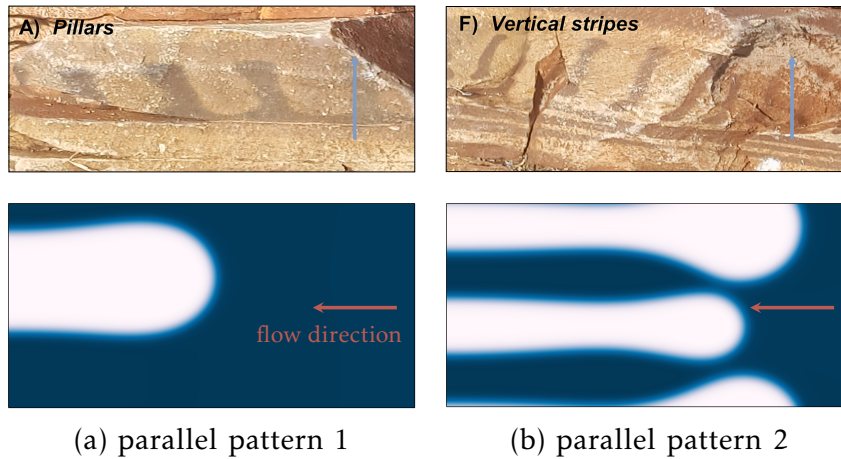
365 **Figure 11.** (a) Concentration profiles along the x -axis for four initial concentrations ranging
 366 from 0.15 and 0.1 to 0.5 with a 0.1 increment with constant transport velocity $v=0.5$. (b) The
 367 estimated banded thickness from the simulations and the corresponding linear fit.

382 The transport velocity and the initial concentration influence the thickness of uni-
 383 form bands. The morphology phase diagram in Figure 5 shows in the column correspond-
 384 ing to $v = 0.5$ for various initial concentrations ($c_{in}=0.1, 0.2$, and 0.3). We quanti-
 385 tatively investigate this relationship using additional simulations with an initial concen-
 386 tration of $c_{in} = 0.15$ and the same fluid speed of $v = 0.5$. Figure 11a displays the concen-
 387 tration profile along the x -axis, enabling the measurement of the mean band thick-
 388 ness. By determining the average band thickness for each simulation, we can establish
 389 a correlation between the parameter c_{in} and the band thickness, as shown in Figure 11b.
 390 The band thickness decreases as the initial concentration increases, displaying an almost
 391 linear relationship.

392 3.3 Zebra rock pattern comparison

393 This section replicates the hematite patterns observed in Zebra rocks from the West-
 394 ern Australian East Kimberley region. We compare the primary features captured by
 395 our simulations with those present in the field patterns for different pattern classifica-
 396 tions, such as parallel, orthogonal, oblique, and spotted patterns. Our primary focus is
 397 to reproduce the diverse morphologies observed in Zebra rocks. However, a quantitative
 398 analysis is beyond the scope of the current research. For further details, see our recent
 399 work that accurately replicates orthogonal banded patterns in Zebra rocks (C. Liu et al.,
 400 2023a).

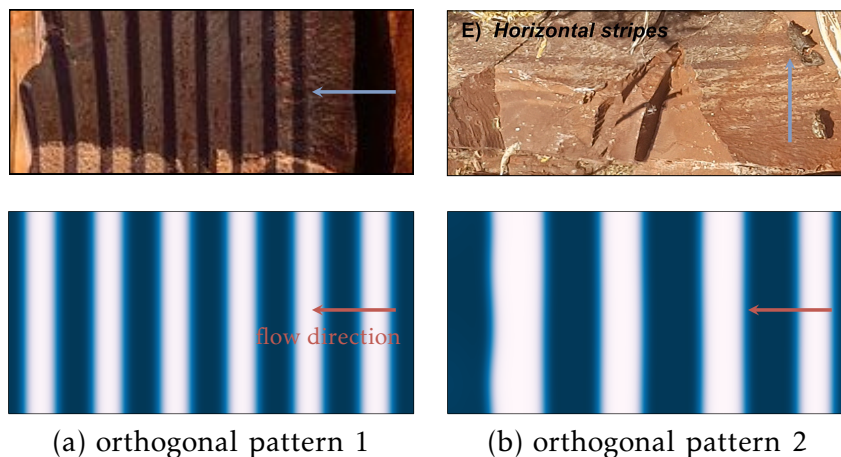
404 *Parallel bands* represent the stripes aligned parallel to the direction of Fe-bearing
 405 flow. Field exploration conducted by Coward and co-authors (Coward et al., 2023) in
 406 four Zebra rock deposits reveals that this pattern is exclusively observed in the Remote
 407 Island outcrop. The researchers identified two representatives within this category: pil-
 408 lars and vertical stripes. Our simulations indicate that these representatives can be clas-
 409 sified as parallel bands with varying propagation lengths. We replicate the two Zebra
 410 rock samples and determine the corresponding flow speeds and initial concentrations by
 411 comparing the simulated morphologies in the morphology phase diagram of Figure 5. The
 412 inverted parameters have the same front velocity $v = 0.05$ and the different initial con-
 413 centrations $c_{in} = 0.5$ for sample 1 and $c_{in} = 0.5$ for sample 2, respectively, as shown
 414 in Figure 12.



401 **Figure 12.** Comparison between the hematite parallel patterns in Zebra rocks and our sim-
 402 ulated patterns. The top two Zebra rock samples are from the Remote Island outcrop, adapted
 403 from Coward et al. (2023). The arrow denotes the Fe-bearing flow direction in each figure.

415 Our inversion indicates that parallel bands emerge under conditions of low fluid ve-
 416 locities. The relatively slow fluid velocity, coupled with a high initial concentration, pro-
 417 motes the formation of elongated strips. On the other hand, a low concentration facil-
 418 itates the development of flat stripes. Consequently, our findings suggest that the trans-
 419 port velocity in the Remote Island outcrop may be relatively sluggish compared to other
 420 locations. Furthermore, inhomogeneous initial conditions can give rise to the simulta-
 421 neous occurrence of both elongated and flat bands.

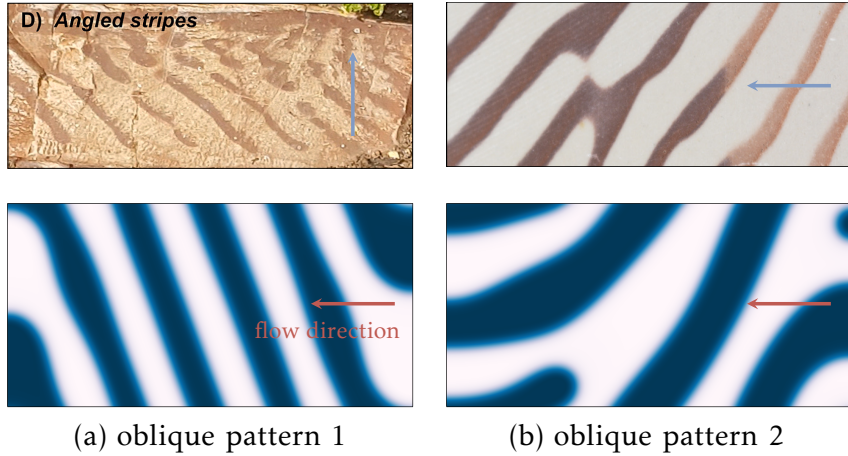
425 *Orthogonal bands* are perpendicular to the fluid direction, commonly observed in
 426 various outcrops. Based on field observations, two orthogonal stripes can be distinguished
 427 in Figure 13. The first group consists of uniform bands with nearly uniform band thick-
 428 ness, as discussed in Section 3.2.4. The second group comprises Liesegang strips that ex-
 hibit an increasing bandwidth along the flow direction, as Section 8 describes.



422 **Figure 13.** Comparison between the hematite orthogonal patterns in Zebra rocks and our
 423 simulated patterns. The top-right Zebra rock sample is located at the Donkey Road deposit,
 424 while the top-right one is from the Remote Island outcrop, adapted from Coward et al. (2023).

429 Following the same procedure as in the previous comparison, we identify the cor-
 430 responding orthogonal stripes that resemble the field morphologies in Figure 5. For the
 431 uniform bands, parameters $v = 0.5$ and $c = 0.2$ produce a similar pattern as shown
 432 in Figure 13. When the velocity is increased to $v = 1.0$ while keeping $c = 0.2$ constant,
 433 our simulation results in a Liesegang pattern. Thus, although we compare field and simu-
 434 lated patterns visually, a quantitative analysis is possible, e.g., in C. Liu et al. (2023a).
 435 Nevertheless, by exploring the morphology phase diagram in Figure 5, we deduce that
 436 the uniform bands indicate a lower transport velocity than the Liesegang patterns. Thus,
 437 our study might suggest that the transport velocity for the uniform pattern observed in
 438 Donkey Road is lower than that for the Liesegang bands observed in the Remote Island.

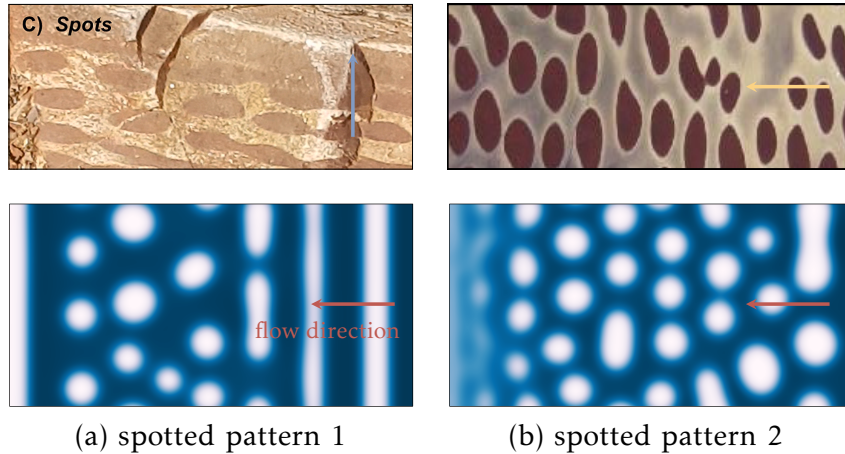
442 *Oblique bands* are stripes inclined relative to the fluid front, as Figure 14 depicts.
 443 The appearance of oblique patterns occurs in field observation and analogous simulations.
 444 Previously, we explained this pattern as a consequence of curved diffusion directions (C. Liu
 445 et al., 2023a), which could be applicable in specific geological situations. However, this
 446 study relaxes the constraint of curved transport velocity for the inclined stripes, allow-
 447 ing them to emerge more efficiently, mimicking a geological setting. Alternatively, the
 448 competition between parallel and orthogonal bands could contribute to the forming of
 oblique bands, as suggested by the transition morphology in Figure 5.



439 **Figure 14.** Comparison between the hematite oblique patterns in Zebra rocks and our simu-
 440 lated patterns. The top-right Zebra rock sample is from the Remote Island outcrop (after Coward
 441 et al. (2023)), while the top-right one is photographed from the Western Australia Museum.

449
 450 Next, we investigate parameter combinations for two Zebra rock samples from the
 451 Remote Island and the Western Australian Museum. Figure 14 demonstrates that fluid
 452 transport velocities of $v = 0.45$ and $v = 0.5$, along with a vanishing initial concentra-
 453 tion $c_{in} = 0.0$, yield comparable oblique bands in the two Zebra rock samples. Inter-
 454 estingly, the field pattern exhibits a branching behavior in some bands, which is also cap-
 455 tured in our results in Figure 14b. Furthermore, while two velocities explain different
 456 patterns in our study, the presence of oblique patterns is heavily influenced by the noise
 457 term η , as Figure 7c shows. Consequently, velocities ranging from 0.45 to 0.5 will likely
 458 result in oblique patterns, with the inclined angle pattern depending on the initial noise
 459 distribution. Nevertheless, the narrowed range of velocities may provide insight into the
 460 potential geological environments during the formation of oblique patterns.

464 *Spotted patterns* combine stripes and spots and patterns consisting solely of spots.
 465 Figures 15a and 15b depict the two types of spotted patterns: (i) stripes that separate
 466 into connected spots and (ii) fully developed isolated spots. Our simulations indicate that
 467 higher fluid speeds contribute to the emergence of mixed patterns. Furthermore, the spot-
 468 ted patterns tend to appear when the initial concentration c_{in} falls within the range of
 0.2 to 0.4, and the fluid speed v exceeds 0.5.



461 **Figure 15.** Comparison between the hematite spotted patterns in Zebra rocks and our simu-
 462 lated spots. The top-right Zebra rock sample is from the Remote Island outcrop (after Coward et
 463 al. (2023)), while the top-right one is located at the Donkey Load deposit.

469
 470 Our simulated morphologies determine the optimal parameters to produce mor-
 471 phologies similar to those in the Museum samples are $v = 5.0$ and $c_{\text{in}} = 0.4$ for sam-
 472 ple 1 of the Remote Island, and $v = 1.0$ and $c_{\text{in}} = 0.4$ for sample 2 of the Donkey Road.
 473 The quantified parameters suggest that the transport velocity in Donkey Road is lower
 474 than that for the Liesegang bands observed in the Remote Island. Additionally, our model
 475 successfully simulates the Ostwald ripening phenomenon, where the stripes separate into
 476 connected and isolated spots in both simulations. This phenomenon plays a crucial role
 477 in the pattern transition observed in Zebra rocks, as discussed in our recent work (C. Liu
 478 et al., 2023a).

479 4 Discussion

480 In this contribution we explored a new framework to explain the diverse patterns
 481 observed in Zebra rocks. This framework builds on the idea of self-organization through
 482 a process similar to the Liesegang phenomenon, where chemicals organize themselves into
 483 bands. Our approach combines the Liesegang theory with a concept from material sci-
 484 ence called phase separation. We modify a well-established model (Cahn-Hilliard) by adding
 485 the effect of flowing groundwater (advection) to mimic how iron oxide dissolves and moves
 486 through rock. This improved model successfully reproduces the variety of patterns seen
 487 in Zebra rocks. The model reveals that it is important to distinguish these Zebra rock
 488 patterns from classic Liesegang bands. Classic Liesegang patterns typically have bands
 489 or rings that increase in width and spacing as they move away from their starting point.
 490 Zebra rocks, however, exhibit a much wider range of patterns, including bands, rods, and
 491 ellipses. We therefore refer to them as Liesegang-like patterns.

492 For the transport-limited case the observed morphological variations between the
 493 Liesegang-like patterns identify differing geological environments during the pattern-forming
 494 process, emphasizing just two factors: the initial solute concentration c_{in} and the fluid
 495 flow velocity v . By systematically examining the parameter space of c_{in} and v using our
 496 model, we can generate all variations of the Liesegang-like patterns previously identified.
 497 However, the impact of geological parameters on the band characteristics varies depend-
 498 ing on the specific category of Liesegang-like patterns being considered. For example,
 499 an oblique banding occurrence most probably indicates the vanishing initial solute con-
 500 centration before the infiltration of acidic iron-bearing fluids. When the Fe-bearing fluid
 501 flow speed narrows to a limited region, the oblique patterns emerge due to the compet-
 502 ing growth of orthogonal and parallel bands. Additionally, the arbitrary inclination an-
 503 gles of the oblique bands may be attributed to the heterogeneous geological conditions
 504 represented by the noise term when setting the initial solute concentration vanish. Our
 505 findings provide insight into the development of randomly oblique patterns observed in
 506 Zebra rocks at five outcrop locations (Coward et al., 2023).

507 One of the categories of orthogonal bands obeys the spacing and width laws com-
 508 monly observed in traditional Liesegang banding. We have previously replicated this type
 509 of pattern, referred to as Liesegang banding, using a pure diffusion-based Cahn-Hilliard
 510 formulation. However, we still classify it as a type of Liesegang-like pattern because the
 511 advection-based formulation annihilates the time law which is primarily governed by diffusion-
 512 limited transport (C. Liu et al., 2022). Our simulations reveal that multiple bands emerge
 513 behind the advection front, unlike the classic Liesegang phenomenon, where band thick-
 514 ness increases step by step. The Ostwald ripening process gradually causes neighboring
 515 bands to coarsen, eventually leading to characteristics similar to those observed in Liesegang
 516 banding.

517 The existence of a linear correlation between the uniform thickness of orthogonal
 518 bands and two controlling parameters presents a valuable opportunity for interpreting
 519 the geological context. Our simulations indicate that the band thickness decreases lin-
 520 early with increasing fluid speed; a similar correlation can be found with the initial so-
 521 lute concentration, too. These quantitative relationships allow us to estimate the fluid
 522 flow rates and initial concentrations based on photographic images captured in the field.
 523 However, a quantitative comparison of the field patterns with the simulated morphologies
 524 is out of the scope of current study. The operational procedure for deriving the dif-
 525 fusion coefficient from orthogonal Zebra rock patterns has been extensively demonstrated
 526 in our earlier work (C. Liu et al., 2023a).

527 The rods and ellipses observed in Zebra rock likely represent an intermediate Ost-
 528 wald Ripening stage, wherein stripes gradually localize into spots or individual spots coarsen
 529 into more prominent spots over time. The former is likely a result of the imposed het-
 530 erogeneity. At the same time, the latter serves to reduce overall system energy, where
 531 combined rods or ellipses are energetically favorable compared to smaller individual spots (Ostwald,
 532 1902). Although our phase separation model can replicate irregular pattern categories,
 533 we cannot exclude the possibility of geological deformation occurring after pattern for-
 534 mation (Sheldon & Retallack, 2001; Retallack, 2021). For instance, formation compaction
 535 may cause spheroids to reduce, resulting in an elliptical shape, a common occurrence in
 536 geological settings. Additional field and experimental work is necessary to confirm the
 537 potential impact of compaction on pattern formation.

538 The examined Zebra rock outcrops exhibit distinct pattern features that have the
 539 potential to provide valuable information about chemical conditions and iron transport.
 540 First, parallel and orthogonal patterns can be observed in different layers of the Ran-
 541 ford formation, attributed to variations in the infiltrating flow rate into the rock. Re-
 542 ferring to the morphology phase diagram (see Figure 5), we can interpret that the fluid
 543 flow rate in the parallel banding layer is lower than that in the orthogonal layer. Ma-
 544 terial heterogeneity, such as permeability, may contribute to these differences in flow rate,

545 as the patterns are bounded by bedding planes. Similarly, inhomogeneous initial con-
 546 ditions can give rise to the simultaneous occurrence of both elongated and flat bands ob-
 547 served in the Remote Island. Furthermore, the variations in pattern features can be used
 548 to infer the flow conditions during the pattern formation process.

549 Zebra rocks, while beautiful and often used as decorative stones, hold a deeper se-
 550 cret. Understanding the patterns of hematite (iron-oxide) within them can unlock valu-
 551 able geological information. These patterns reveal the complex interplay between chem-
 552 ical reactions and fluid movement that shaped the rock. Similar processes may have been
 553 at work in the distant past, creating features like the early Earth's banded iron forma-
 554 tions (BIFs) and the hematite spherules found on Mars. For instance, iron oxide spots
 555 and rods found in Earth's Navajo Sandstone are considered a close match to hematite
 556 nodules on Mars (Chan et al., 2004; Yoshida et al., 2018). The insights gained from study-
 557 ing Zebra rocks may therefore provide valuable tools for interpreting data and poten-
 558 tially even detecting signs of past life on Mars.

559 The Precambrian Banded Iron Formations (BIFs) show three scales of bandings
 560 that may have self-organizational origins (Wang et al., 2009). Understanding how Ze-
 561 bra rock patterns form has significant implications beyond just Zebra rocks themselves.
 562 It can help us unlock secrets about Earth's history and potentially guide resource ex-
 563 ploration. BIFs, similar to Zebra rocks in pattern formation but with a higher iron con-
 564 tent, are commercially valuable for iron ore. By studying Zebra rocks with our model,
 565 methods that identify promising BIF deposits using aerial photographs or drone images
 566 may be developed. This could be a game-changer for resource exploration. The abun-
 567 dance of BIFs in the Archaean and early Proterozoic eras, followed by their decline, sug-
 568 gests a significant shift in the ocean environment. Using our simulations to translate ob-
 569 served patterns into geological parameters guides the potential development of entirely
 570 new geophysical tools. These tools could help us reconstruct the conditions on early Earth's
 571 crust, offering a glimpse into our planet's distant past.

572 5 Conclusion

573 This study delves into the intriguing patterns found in Zebra rocks, focusing on how
 574 these patterns form over time. We use a computer model that simulates the separation
 575 of iron oxide (hematite) under flowing water (advective phase separation). This model
 576 provides valuable insights into how two key factors influence the shapes and transitions
 577 of these patterns: (i) how the iron oxide is initially distributed within the rock affects
 578 the resulting patterns; (ii) the speed at which water moves through the rock plays a role
 579 in shaping the patterns.

580 Using our simulations, we were able to categorize the resulting patterns (referred
 581 to as Liesegang-like patterns) and quantify the influence of the two factors mentioned
 582 above. Here are some key findings: (i) we were able to recreate the spacing and width
 583 of various Liesegang-like patterns based on the initial iron oxide distribution and water
 584 flow velocity; (ii) lower initial iron oxide concentration seems to favor the formation of
 585 slanted patterns, and the angle of the slant can reveal information about the rock's in-
 586 ternal structure; (iii) for straight, banded patterns, we identified a linear relationship be-
 587 tween the controlling factors and the thickness of the bands.

588 Our classification system allows us to match simulated patterns with those observed
 589 in the field. This "reverse analysis" helps us to estimate the key parameters that con-
 590 trol pattern formation in different Zebra rock locations. By comparing simulated pat-
 591 terns with real-world observations, we found a close resemblance, suggesting the model's
 592 accuracy. This paves the way for a powerful tool: a computer-aided interpretation frame-
 593 work. This tool can analyze patterns captured in field photographs, similar to Zebra rocks.
 594 We can then estimate crucial geochemical parameters that were present when the pat-

595 terns formed, including the chemical makeup and water flow conditions. The model's ca-
 596 pability to interpret past environments is particularly valuable for understanding the con-
 597 ditions on early Earth and Mars. By analyzing patterns in rocks from these locations,
 598 we can potentially uncover clues about the chemical conditions and fluid movement that
 599 existed billions of years ago.

600 6 Open Research

601 The Finite Element Method code and numerical results will be available after peer
 602 review.

603 Acknowledgments

604 The authors wish to acknowledge the generous support of the Western Australian Mu-
 605 seum for the supply of the high quality images of Zebra Rock in particular Geoff Dea-
 606 con for taking the photos and the curator Peter Downes for managing the request. The
 607 support of the Research Grant Council of Hong Kong (ECS 27203720 and GRF 17206521)
 608 and the Australian Research Council (ARC DP200102517, DP170104550, LP170100233)
 609 is acknowledged.

610 References

- 611 Al-Ghoul, M., & Sultan, R. (2019). Simulation of geochemical banding: Theoretical
 612 modeling and fractal structure in acidization-diffusion-precipitation dynamics.
 613 *Physical Review E*, *100*(5), 052214.
- 614 Antal, T., Droz, M., Magnin, J., & Rácz, Z. (1999). Formation of Liesegang pat-
 615 terns: A spinodal decomposition scenario. *Physical Review Letters*, *83*(15),
 616 2880.
- 617 Arndt, D., Bangerth, W., Blais, B., Clevenger, T. C., Fehling, M., Grayver, A. V.,
 618 ... Wells, D. (2020). The deal.II Library, Version 9.2. *Journal of Numerical*
 619 *Mathematics*, *28*(3), 131-146.
- 620 Arvidson, R., Squyres, S., Bell III, J., Catalano, J., Clark, B., Crumpler, L., ... oth-
 621 ers (2014). Ancient aqueous environments at Endeavour crater, Mars. *Science*,
 622 *343*(6169), 1248097.
- 623 Barge, L., Hammond, D., Chan, M., Potter, S., Petruska, J., & Nealon, K. (2011).
 624 Precipitation patterns formed by self-organizing processes in porous media.
 625 *Geofluids*, *11*(2), 124-133.
- 626 Cahn, J. W. (1961). On spinodal decomposition. *Acta Metallurgica*, *9*(9), 795-801.
- 627 Cahn, J. W., & Hilliard, J. E. (1958). Free Energy of a Nonuniform System. I. Inter-
 628 facial Free Energy. *The Journal of Chemical Physics*, *28*(2), 258-267.
- 629 Chan, M. A., Beitler, B., Parry, W., Ormö, J., & Komatsu, G. (2004). A possi-
 630 ble terrestrial analogue for haematite concretions on mars. *Nature*, *429*(6993),
 631 731-734.
- 632 Coward, A. J., Slim, A. C., Brugger, J., Wilson, S., Williams, T., Pillans, B., &
 633 Maksimenko, A. (2023). Mineralogy and geochemistry of pattern formation
 634 in zebra rock from the East Kimberley, Australia. *Chemical Geology*, *622*,
 635 121336.
- 636 DeWitt, S., Rudraraju, S., Montiel, D., Andrews, W. B., & Thornton, K. (2020).
 637 PRISMS-PF: A general framework for phase-field modeling with a matrix-free
 638 finite element method. *npj Computational Materials*, *6*(1), 1-12.
- 639 Foard, E., & Wagner, A. (2012). Survey of morphologies formed in the wake of an
 640 enslaved phase-separation front in two dimensions. *Physical Review E*, *85*(1),
 641 011501.
- 642 Furukawa, H. (1992). Phase separation by directional quenching and morphologi-
 643 cal transition. *Physica A: Statistical Mechanics and its Applications*, *180*(1-2),

- 644 128–155.
- 645 Geidans, L. (1981). Zebra rock of Western Australia. In *Geological Society of Aus-*
646 *tralia, Abstracts* (Vol. 3, p. 22).
- 647 Hu, M., Sun, Q., Schrank, C., & Regenauer-Lieb, K. (2022). Cross-scale dynamic
648 interactions in compacting porous media as a trigger to pattern formation. *Geo-*
649 *physical Journal International*, 230(2), 1280–1291.
- 650 Ishikawa, R., Tani, M., & Kurita, R. (2022). Three-dimensional phase separation
651 under a nonstationary temperature field. *Physical Review Research*, 4(3),
652 033152.
- 653 Kawahara, H., Yoshida, H., Yamamoto, K., Katsuta, N., Nishimoto, S., Umemura,
654 A., & Kuma, R. (2022). Hydrothermal formation of Fe-oxide bands in zebra
655 rocks from northern Western Australia. *Chemical Geology*, 590, 120699.
- 656 Krekhov, A. (2009). Formation of regular structures in the process of phase separa-
657 tion. *Physical Review E*, 79(3), 035302.
- 658 Larcombe, C. (1926). Some rocks from four miles east of Argyle Station, Ord River,
659 King district, Kimberley division. *Geological Survey of Western Australia, An-*
660 *ual Report*, 23.
- 661 L’Heureux, I. (2013). Self-organized rhythmic patterns in geochemical systems.
662 *Philosophical Transactions of the Royal Society A: Mathematical, Physical and*
663 *Engineering Sciences*, 371(2004), 20120356.
- 664 Liu, B., Zhang, H., & Yang, Y. (2000). Surface enrichment effect on the morphologi-
665 cal transitions induced by directional quenching for binary mixtures. *The Jour-*
666 *nal of Chemical Physics*, 113(2), 719–727.
- 667 Liu, C., Calo, V., Regenauer-Lieb, K., & Hu, M. (2023a). Coefficients of reaction-
668 diffusion processes derived from patterns in rocks. *Journal of Geophysical Re-*
669 *search: Solid Earth*, 128(5), e2022JB026253.
- 670 Liu, C., Calo, V. M., Regenauer-Lieb, K., & Hu, M. (2023b). Dendritic growth
671 patterns in rocks: Inverting the driving and triggering mechanisms. *Journal of*
672 *Geophysical Research: Solid Earth*, 128(9), e2023JB027105.
- 673 Liu, C., Hu, M., & Regenauer-Lieb, K. (2022). Liesegang Patterns Interpreted as a
674 Chemo-Hydromechanical Instability. In *Multiscale Processes of Instability, De-*
675 *formation and Fracturing in Geomaterials: Proceedings of 12th International*
676 *Workshop on Bifurcation and Degradation in Geomechanics* (pp. 59–66).
- 677 Loughnan, F., & Roberts, F. (1990). Composition and origin of the ‘zebra rock’ from
678 the East Kimberley region of Western Australia. *Australian Journal of Earth*
679 *Sciences*, 37(2), 201–205.
- 680 Mattievich, E., Chadwick, J., Cashion, J., Boas, J., Clark, M., & Mackie, R. (2003).
681 Macroscopic ferromagnetic liquid crystals determine the structure of Kimberley
682 zebra rock. In *Proceedings of the 27th Annual A&NZIP Condensed Matter and*
683 *Materials Meeting* (pp. 1–3).
- 684 Ortoleva, P. J., Merino, E., Moore, C., & Chadam, J. (1987). Geochemical self-
685 organization i; reaction-transport feedbacks and modeling approach. *American*
686 *Journal of Science*, 287(10), 979–1007.
- 687 Ostwald, W. (1902). *Lehrbuch der allgemeinen Chemie* (Vol. 2). W. Engelmann.
- 688 Qiu, W. J., Zhou, M.-F., & Williams-Jones, A. E. (2024). Numerical Simulation of
689 the Self-Organizational Origin of Concentrically Zoned Aggregates of Siderite
690 and Pyrite in Sediment-Hosted Massive Sulfide Deposits. *Journal of Geophys-*
691 *ical Research: Solid Earth*, 129(3), e2023JB028101.
- 692 Retallack, G. (2021). Zebra rock and other Ediacaran paleosols from Western Aus-
693 tralia. *Australian Journal of Earth Sciences*, 68(4), 532–556.
- 694 Sheldon, N. D., & Retallack, G. J. (2001). Equation for compaction of paleosols due
695 to burial. *Geology*, 29(3), 247–250.
- 696 Tsukada, T., & Kurita, R. (2020). Mechanism behind columnar pattern forma-
697 tion during directional quenching-induced phase separation. *Physical Review*
698 *Research*, 2(1), 013382.

- 699 Wang, Y., Chan, M. A., & Merino, E. (2015). Self-organized iron-oxide cementation
700 geometry as an indicator of paleo-flows. *Scientific Reports*, *5*(1), 1–15.
- 701 Wang, Y., Xu, H., Merino, E., & Konishi, H. (2009). Generation of banded iron
702 formations by internal dynamics and leaching of oceanic crust. *Nature Geo-*
703 *science*, *2*(11), 781–784.
- 704 Yatsuda, Y., Tsushima, K., Fang, Q., & Nabika, H. (2023). Chemical Model for
705 Pattern Formation in Rocks via Periodic Precipitation of Iron Oxide Minerals.
706 *ACS Earth and Space Chemistry*, *7*(10), 2042–2049.
- 707 Yoshida, H., Hasegawa, H., Katsuta, N., Maruyama, I., Sirono, S., Minami, M., . . .
708 others (2018). Fe-oxide concretions formed by interacting carbonate and acidic
709 waters on Earth and Mars. *Science Advances*, *4*(12), eaau0872.
- 710 Yoshida, H., Katsuta, N., Sirono, S.-i., Nishimoto, S., Kawahara, H., & Metcalfe, R.
711 (2020). Concentric Fe-oxyhydroxide bands in dacite cobbles: Rates of buffering
712 chemical reactions. *Chemical Geology*, *552*, 119786.